Check for updates

JGR Solid Earth

RESEARCH ARTICLE
10.1029/2021JB023532

Azimuthally Anisotropic Structure in the Crust and Uppermost Mantle in Central East China and Its Significance to Regional Deformation Around the Tan-Lu Fault Zone

Terhemba Shadrach Bem[1,2], Chuanming Liu[3], Huajian Yao[1,4,5], Song Luo[1], Yuan Yang[1], and Bin Liu[1,4]

[1]Laboratory of Seismology and Physics of Earth's Interior, School of Earth and Space Sciences, University of Science and Technology of China, Hefei, Anhui, China, [2]Department of Physics, Federal University Duste, Dutse, Jigawa State, Nigeria, [3]University of Colorado, Boulder, CO, USA, [4]Mengcheng National Geophysical Observatory, University of Science and Technology of China, Anhui, China, [5]CAS Center for Excellence in Comparative Planetology, USTC, Hefei, Anhui, China

Key Points:

- Azimuthal anisotropy in the crust and uppermost mantle deviates from stress, shear-wave splitting, and absolute plate motion direction
- Within proximity of regional faults, anisotropy might be related to fault fabrics including fractures that strike parallel to the fast axes
- The direction of anisotropy coincides with the strike of the Tan-Lu Fault signifying structural sources in the crust and uppermost mantle

Supporting Information:

Supporting Information may be found in the online version of this article.

Correspondence to:

H. Yao,
hjyao@ustc.edu.cn

Citation:

Bem, T. S., Liu, C., Yao, H., Luo, S., Yang, Y., & Liu, B. (2022). Azimuthally anisotropic structure in the crust and uppermost mantle in central East China and its significance to regional deformation around the Tan-Lu Fault zone. *Journal of Geophysical Research: Solid Earth*, *127*, e2021JB023532. https://doi.org/10.1029/2021JB023532

Received 31 OCT 2021
Accepted 17 FEB 2022

Author Contributions:

Conceptualization: Chuanming Liu, Huajian Yao
Data curation: Terhemba Shadrach Bem, Huajian Yao, Song Luo, Yuan Yang
Formal analysis: Terhemba Shadrach Bem
Funding acquisition: Huajian Yao, Bin Liu
Investigation: Terhemba Shadrach Bem, Song Luo
Methodology: Chuanming Liu
Project Administration: Huajian Yao, Bin Liu
Resources: Huajian Yao
Software: Chuanming Liu, Huajian Yao
Supervision: Huajian Yao
Validation: Terhemba Shadrach Bem, Song Luo

© 2022. American Geophysical Union. All Rights Reserved.

Abstract Seismic anisotropy can be linked to different mechanisms, structures, and sources. We constrained the 3-D depth-dependent shear wave speed isotropic and azimuthally anisotropic structures with Rayleigh wave phase velocity from ambient noise in central Eastern China. We compared the results with other models and found that in the upper crust, the maximum horizontal stress direction differs mainly from the anisotropy that coincides with the strikes of major faults and geologic structures. We inferred that the anisotropy within proximity of faults might be related to fault fabrics, including fractures that strike parallel to the fast axes. The Tan-Lu Fault controls the anisotropy in the crust to the uppermost mantle. The direction of fast axes in the fault zone is NNE-SSW to N-S, coinciding with the fault strike and trend that matches the fault shape on the surface. Southeastern North China craton has a weak anisotropy in the crust and uppermost mantle. The sources are possibly connected to the thrusting, tight trending folds, and dipping thrusts observed to be sub-parallel to the Dabie Orogenic Belt (DOB). We propose that the NNE-SSW Zhangbaling uplift group comes from the extension and ductile shearing in the Tan-Lu Fault zone and the dragging of the northeastern South China Craton in the crust and the uppermost mantle. The N-S polarized fast axes in the lower crust and uppermost mantle across the Sulu orogen and Xuzhou thrust-and-fold belt are the products of the resultant effect of subduction and deep Tan-Lu faulting.

Plain Language Summary Seismic anisotropy is the dependence of seismic velocity of the medium on wave propagation direction. When observed, it gives information about the nature of material deformation. We used surface waves recovered from background noise to determine the anisotropy and its connection to the Tan-Lu fault system, the largest fault system in Eastern China. Our results show that seismic anisotropy in the upper crust is likely caused by fault zone fabrics and the regional stress field. In the middle crust to the uppermost mantle, the anisotropy is parallel to the strike of the Tan-Lu fault, indicating that the fault penetrates to the uppermost mantle and controls the anisotropy. The southeastern North China craton has weak anisotropy in the crust and uppermost mantle. The cause of anisotropy is likely the thrust faults resulting from compression that strike similar to the trend of the Dabie Orogenic Belt. The extension and shearing in the Tan-Lu Fault zone is likely what caused the anisotropy at Zhangbaling uplift. The direction of anisotropy changes to N-S in the north of the study region in the lower crust and uppermost mantle. The cause might be related to the resultant effect of subduction and deep Tan-Lu faulting.

1. Introduction

The interactions between the crust and the mantle have many effects on the lithosphere, such as lithospheric destruction, seismicity, magmatism, and fault activation. The lithosphere in East China is a famous tectonic laboratory where these effects have been studied for decades. At the moment, the lithosphere in East China is associated with magmatism, widespread lithospheric thinning (e.g., L. Chen et al., 2006, 2014; Cheng et al., 2013; Fu et al., 2016; Z. Liu et al., 2016; Y. Yang et al., 2018) and seismicity (e.g., Deng et al., 2013; Lin et al., 1998; D. Yao et al., 2017 , 2016; P. Zhao et al., 2018). In central-East China, the North China Craton (NCC) and the South China Craton (SCC) collided in the Mesozoic, resulting in the subduction of the SCC beneath NCC (Faure et al., 2003; Hacker et al., 2000). This interaction is believed to have produced tectonic structures such as the

Visualization: Terhemba Shadrach Bem
Writing – original draft: Terhemba Shadrach Bem
Writing – review & editing: Terhemba Shadrach Bem, Chuanming Liu, Huajian Yao, Song Luo, Yuan Yang, Bin Liu

Dabie Orogenic Belt (DOB), Sulu Orogenic Belt (SOB), Tan-Lu Fault (TLF) zone, and others, with their evolution, still a subject of constant debate. It is proposed that the TLF is a lithospheric fault, and its presence in East China could have played a critical role in lithospheric instabilities (L. Chen et al., 2006) and may also control the crustal anisotropy in the region. The investigation of this claim is sketchy, especially in central East China, where the TLF zone, NCC, and SCC are considered to be in geodynamic interaction. Constraining the anisotropy in the crust and uppermost mantle and the affinity of the TLF zone to the anisotropy is critical to resolving some of the ongoing debate regarding the tectonic evolution and the geodynamic interplay between tectonic units in East China. One of the critical research questions this work seeks to answer is to what extent does TLF zone controls the anisotropy in central-eastern China relative to the regional deformation history?

Seismic anisotropy is the directional variation of intrinsic elastic properties when measured at a point in a medium. The nature and depth of anisotropy are controlled by the shape or Lattice Preferred Orientation (LPO) of anisotropic minerals (Crampin & Peacock, 2008; Savage, 1999) and also, the fault fabrics or shearing in fault zones in the crust (Balfour et al., 2005; Boness & Zoback, 2006). The sources of seismic anisotropy in the crust are not completely clear due to the complex structure of the crust (Balfour et al., 2005). Nevertheless, studies have demonstrated that seismic anisotropy in the upper crust is associated mainly with the alignment of fluid-filled micro-cracks in the layer due to ambient stress (Crampin & Peacock, 2008; Y. Yang et al., 2018). Within proximity to major strike-slip faults, measurement of anisotropy reveals that frictionally weak faults may have local control on seismic anisotropy (Balfour et al., 2005; Boness & Zoback, 2006). In the middle to lower crust, identified anisotropy is often linked to the preferred orientations of minerals, mainly biotite and amphibole (Weiss et al., 1999). While observed anisotropy in the mantle is associated with the LPO of Olivine, an anisotropic mineral that is abundant in the upper mantle (Fouch & Rondenay, 2006; Savage, 1999; Tian & Santosh, 2015).

The sources and depths of observed anisotropic have been constrained using different seismological techniques and datasets at local, regional, and global scales with varying degrees of resolutions and limitations (e.g., Cheng et al., 2013; Fu et al., 2016; C. Liu et al., 2019; Tian & Santosh, 2015; H. Yao, 2015; H. Yao et al., 2010; L. Zhao et al., 2013; Z. Zhang et al., 2022). In East China, particularly in the NCC, interesting geophysical deformation models have been proposed to offer basic observational constraints for the understanding of the processes and mechanisms of the destruction of the NCC from seismic anisotropy (e.g., Fu et al., 2016; Z. Liu et al., 2016; Y. Yang et al., 2018). However, these results in the NCC did not constrain the deformation in the eastern SCC or explain the geodynamic interactions between NCC, TLF, and the SCC. In an attempt to offer more constraints in central-eastern China, H. Huang et al. (2013) and Y. Yang et al. (2018) employed seismic anisotropy from shear-wave splitting and receiver functions. Their results showed moderately large and averagely small delay times for mantle and crust, respectively (H. Huang et al., 2013; Y. Yang et al., 2018). However, the quantitative estimates and the depths of occurrences of the inferred components of seismic anisotropy were not estimated. Moreover, the anisotropy observed from shear-wave splitting results is understood to be mainly from the upper mantle sources with only a fractional contribution of crustal sources (around 0.1 s per 10 km; Iidaka & Niu, 2001; Shi et al., 2013; C. Y. Wang et al., 2017). By this, to quantify the anisotropy in the crust and uppermost mantle, additional techniques are required. Y. Meng et al. (2019) constrained shear-wave velocity (isotropic) and period-dependent Rayleigh wave phase velocity azimuthal anisotropy in southern-central TLF and surroundings, making it difficult to connect with the depth-domain anisotropy. Depth-dependent shear-wave velocity and azimuthally anisotropic results are obtained beneath Chao Lake in the southern TLF zone from ambient noise tomography using dense short-period array data (Luo & Yao, 2021). Though the findings are impressive, the azimuthal anisotropy results are only for a small region and restricted to the upper crust.

Our study region consists of the southeastern part of the NCC (from Xuzhou to Hefei), the TLF zone, and the northeastern parts of the SCC (Figure 1). Basically, in the north of the study region, the geology is made of the High Pressure (HP) and/or Ultrahigh-Pressure (UHP) rock units beneath the ENE-trending SOB (Hacker et al., 2000; T. Zhao et al., 2016) and the metamorphosed Cretaceous granitoids in the Xuzhou thrust-and-fold belt (Shu et al., 2017). The southern region is characterized by uplifts, depressions, basins, and the southern segment of the TLF zone that is associated with ductile shearing with foliation and stretching lineation in the Zhangbaling uplift (Shu et al., 2017; J. Zhang et al., 2015; T. Zhao et al., 2016, 2014; Zhu et al., 2009). Generally, seismic velocity and earthquake studies reveal the segmentation of velocity and earthquakes distribution in the region (e.g., Bem et al., 2020; Deng et al., 2013; Lin et al., 1998; Y. Meng et al., 2019), which could suggest the reactivation of the TLF zone and a critically deformed lithosphere. Our study took advantage of the dense local

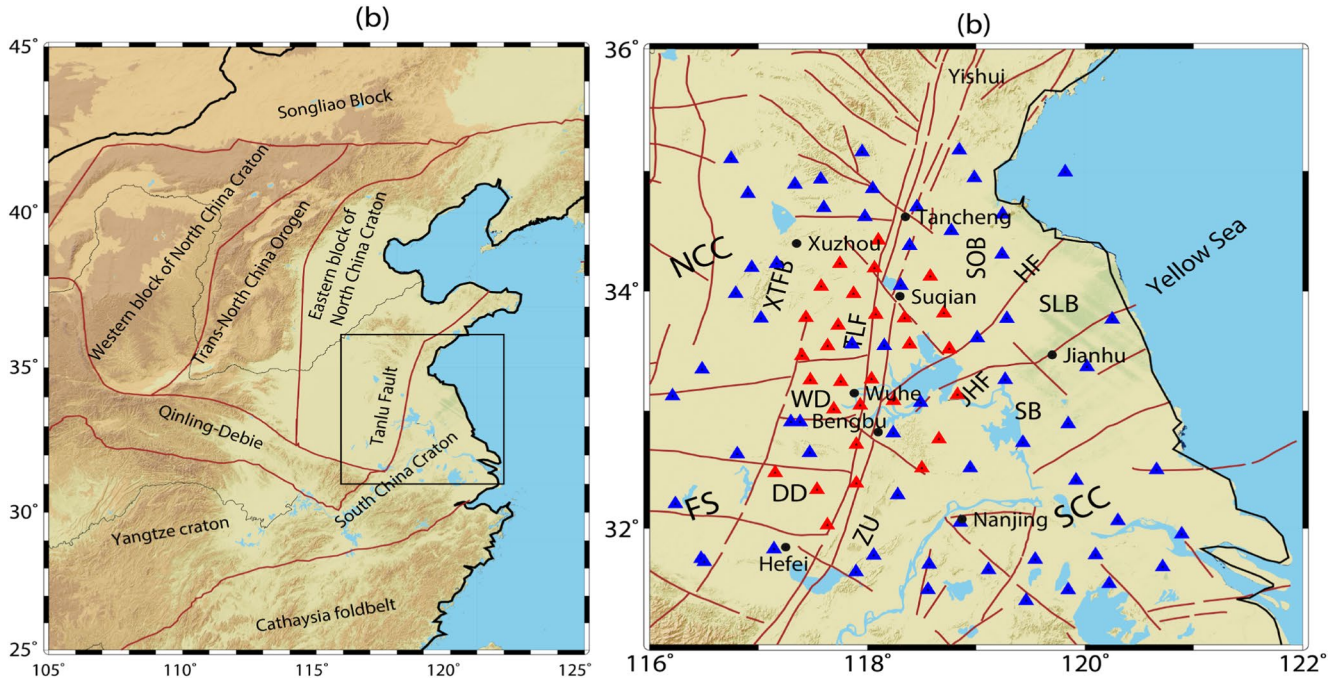

Figure 1. The major regional tectonic blocks in East China, with the study region shown as the black rectangle (a). The study region showing detailed tectonic features and stations distribution (blue and red triangles as permanent and temporary stations respectively) (b): Tan-Lu Fault (TLF); Xuzhou Thrust-and-Fold Belt (XTFB); Sulu Orogenic Belt (SOB); North China Craton (NCC), South China Craton (SCC), Dabie Orogenic Belt (DOB), Zhangbaling Uplift (ZU); Huaiying-Xiangshuokou Fault (HF); Jianhu Hidden Fault (JHF); Subei Basin (SB); Sulu Basin (SLB); Dingyuang Depression (DD); Wuhe Depression (WD); Feizhong Suture (FS). The brown lines are faults, while the black dots are cities.

seismic array (Figure 1b) and ambient noise Rayleigh wave phase velocity dispersion data to produce a high-resolution depth-dependent 3-D model of shear wave speed and azimuthal anisotropy in the crust and the uppermost mantle in central-eastern China. Our model offers a tight constraint on azimuthal anisotropy in the crust and uppermost mantle. By comparing it with shear-wave splitting results, maximum compressional stress field and absolute plate motion in the region, we reveal additional insight into the sources of crustal and uppermost mantle anisotropy relative to the regional deformation across the collision zone of NCC, TLF, and SCC.

2. Data and Method

The continuous seismic data used in this study was obtained from 29 broadband temporary stations and 61 permanent stations. The temporary stations are the University of Science and Technology of China (USTC) deployment, while the permanent stations belong to the China Earthquake Network Center Data Management Center (Figure 1). This data was acquired in 2015–2017, providing a time-series length for each station of at least 2 years. We calculated the ambient noise vertical component cross-correlation and measured the Rayleigh wave phase speeds from 2 to 40 s (Figure S1 in Supporting Information S1). This dataset is the same as used in our previous paper (Bem et al., 2020). For this reason, the details of data processing from single stations to picking of dispersion curves are well discussed in the paper (Bem et al., 2020). In this paper, our main task is to obtain jointly depth-dependent isotropic velocity and azimuthal anisotropy from the measured dispersion curves (Figure S1 in Supporting Information S1).

We adopted the method of DAzimSurfTomo (C. Liu et al., 2019) for direct inversion of Rayleigh wave dispersion speed for 3-D vertically polarized shear-wave speed (*Vsv;* isotropic) and azimuthal anisotropy from mixed-path Rayleigh wave travel time data. This approach considers the frequency-dependent Rayleigh wave ray tracing based on 2-D isotropic phase velocity maps using the fast marching method (Rawlinson & Sambridge, 2004). The forward problem starts from the travel-time equation. Consider a raypath (AB) between two stations A and

B in a heterogeneous medium with the inclusion of azimuthal variation ψ to the phase velocity, the travel time $t_{AB}(\omega)$ can be written as

$$t_{\mathrm{AB}}(\omega) = \int_{l_{\mathrm{AB}}} \frac{1}{c(l,\omega,\psi)} dl, \tag{1}$$

where ω is the frequency and dl is the segment along the raypath AB. Equation 1 can be discretized from which the Rayleigh wave phase velocity $c(\omega,\psi)$, assuming a weak anisotropic medium can be expressed as (Smith & Dahlen, 1973):

$$c(\omega,\psi) = c_0(\omega) + a_1(\omega)cos2\psi + a_2(\omega)sin2\psi + a_3(\omega)cos4\psi + a_4(\omega)sin4\psi, \tag{2}$$

where $c_0(\omega)$ is the isotropic phase speed, $a_{1,2}$ and $a_{3,4}$ are the amplitudes of 2ψ (180° periodicity) and 4ψ (90° periodicity) terms, respectively. We can break Equation 2 into three parts:

$$c(\omega,\psi) = c_0^{ref}(\omega) + \delta c_k^{ETI}(\omega) + \delta c_k^{AA}(\omega,\psi). \tag{3}$$

Here, $c_0^{ref}(\omega)$ is the prediction from reference moduli, $\delta c_k^{ETI}(\omega)$ and $\delta c_k^{AA}(\omega,\psi)$ are respectively the phase velocity perturbation from effective transverse isotropic moduli (ETI) and azimuthally anisotropic moduli (AA) relative to the reference moduli. The study area is parameterized using predefined regular grids from which the travel-time difference between the measurement $t^{obs}(\omega)$ and the isotropic reference model prediction $t^{ref}(\omega)$ at frequency ω can be written as:

$$\delta t(\omega) = t^{obs}(\omega) - t^{ref}(\omega) \approx \sum_{k=1}^{K} \frac{R_k}{\left(c_0^k(\omega)\right)^2} \left(\delta c_k^{ETI}(\omega) + \delta c_k^{AA}(\omega,\psi)\right), \tag{4}$$

where k is the index of the grid point in the model, K is the total number of 2-D grids, R_k is the coefficient of interpolation.

Following C. Liu et al. (2019), Fang et al. (2015), and H. Yao (2015), the isotropic perturbation of Rayleigh wave phase velocity can be expressed as

$$\begin{aligned} \delta c^{ETI}(\omega) &= \int_0^H \left(\frac{\partial c}{\partial A}\delta A + \frac{\partial c}{\partial C}\delta C + \frac{\partial c}{\partial L}\delta L + \frac{\partial c}{\partial F}\delta F\right) dz \\ &\approx \int_0^H \left(\frac{\partial c}{\partial \alpha}\delta\alpha + \frac{\partial c}{\partial \beta}\delta\beta + \frac{\partial c}{\partial \rho}\delta\rho\right) dz, \end{aligned} \tag{5}$$

where $\alpha, \beta,$ and ρ are respectively the compressional wave speed (V_{PH}) of horizontally propagating P-waves, shear wave speed (V_{SV}) of vertically polarized S-waves propagating horizontally, and mass density. The parameters A, C, L, and F (with another, N) represent the transversely isotropic medium. Meanwhile, Montagner and Nataf (1986) and H. Yao (2015) showed that the azimuthally anisotropic perturbation in the Rayleigh wave phase velocity is approximated as

$$\delta c^{AA}(\omega,\ \psi) \approx \int_0^H \left[\left(B_c\frac{\partial c}{\partial A} + G_c\frac{\partial c}{\partial L}\right)cos2\psi + \left(B_s\frac{\partial c}{\partial A} + G_s\frac{\partial c}{\partial L}\right)sin2\psi\right] dz, \tag{6}$$

where $B_c, B_s, G_c,$ and G_s represent the 2ψ azimuthal variations of A and L, respectively (C. Liu et al., 2019; Montagner & Nataf, 1986). We can then substitute Equations 6 and 5 into Equation 4 to obtain the travel time perturbation at all frequencies $\delta t(\omega)$; a solution that can be written in the classical inversion function as

$$\mathbf{d} = \mathbf{Gm} = \mathbf{G}\left[\delta\beta_1(z_1)\ldots\delta\beta_1(z_J)\ldots\delta\beta_k(z_J)\frac{G_c^1(z_1)}{L_1(z_1)}\ldots\frac{G_c^1(z_J)}{L_1(z_J)}\ldots\frac{G_c^K(z_J)}{L_K(z_J)}\frac{G_s^1(z_1)}{L_1(z_1)}\ldots\frac{G_s^1(z_J)}{L_1(z_J)}\ldots\frac{G_s^K(z_J)}{L_K(z_J)}\right]^T \tag{7}$$

where $\boldsymbol{d}$ is the vector of the travel-time residuals, $\boldsymbol{G}$ is the data sensitivity matrix, and $\boldsymbol{m}$ is defined by the transpose of independent parameters, $[\delta\beta, \frac{G_c}{L}, \frac{G_s}{L}]$ given in the square bracket is the model matrix (C. Liu et al., 2019). Equation 7 is solved using the LSQR (Paige & Saunders, 1982) with the regularized inversion system as:

$$\begin{bmatrix} \boldsymbol{G}_{iso} & \boldsymbol{G}_{AA} & \\ \lambda_1 \boldsymbol{L}_{iso} & 0 & \boldsymbol{m}_{iso} \\ 0 & \lambda_2 \boldsymbol{L}_{AA} & \end{bmatrix} \begin{bmatrix} \boldsymbol{m}_{iso} \\ \boldsymbol{m}_{AA} \end{bmatrix} = \begin{bmatrix} \boldsymbol{d} \\ 0 \\ 0 \end{bmatrix}, \tag{8}$$

where $\boldsymbol{L}_{iso}$ and $\boldsymbol{L}_{AA}$ are the isotropic and azimuthally anisotropic roughening matrices, while $\boldsymbol{G}_{iso}, \boldsymbol{G}_{AA}, \boldsymbol{m}_{iso}$, and $\boldsymbol{m}_{AA}$ are the isotropic and azimuthally anisotropic data sensitivity matrices and model parameter vectors, respectively. To balance data fitting and model regularization, we introduce the first-order Tikhonov regularization for both isotropic and anisotropic model parameters, in which weights (λ_1 and λ_2) are obtained by employing the L-curve technique (Hansen et al., 2007; Figure S2 in Supporting Information S1). We searched for the corners taken to be the best weights (λ_1 and λ_2) from a range of weights considered (Figure S2 in Supporting Information S1) that balance the data fitting and model regularization. Finally, the azimuthally anisotropic $\hat{V}_{SV}$ is given by:

$$\hat{V}_{SV} \approx V_{SV}\left(1 + \frac{G_c}{2L}cos2\psi + \frac{G_s}{2L}sin2\psi\right) = V_{SV}[1 + A_{SV}cos2(\psi - \phi)] \tag{9}$$

$$A_{SV} = \frac{1}{2}\sqrt{\left(\frac{G_s}{L}\right)^2 + \left(\frac{G_c}{L}\right)^2} \tag{10}$$

$$\phi = \frac{1}{2}\tan^{-1}\left(\frac{G_s}{L}/\frac{G_c}{L}\right) = \frac{1}{2}\tan^{-1}\left(\frac{G_s}{G_c}\right), \tag{11}$$

where V_{SV} is the isotropic part of $\hat{V}_{SV}$, A_{SV} is the anisotropy amplitude, ϕ is the azimuth of fast polarization.

In practice, our whole workflow is implemented in two steps. Firstly, we got a 3-D isotropic *Vsv* reference model from Bem et al. (2020) which is obtained by employing a 3-D direct inversion method (DSurfTomo; Fang et al., 2015). Then, we perform joint inversion for both isotropic *Vsv* perturbation and azimuthal anisotropy using the DAzimSurfTomo method (C. Liu et al., 2019).

3. Results

3.1. Model Resolution Tests and Reliability

Tomography model resolution and reliability depend significantly on the data coverage, which is often shown by the raypath maps as a function of the period (s; Figure 2). The raypath coverage maps reveal that short periods between 2 and 5 s have relatively sparse coverage except at the center of the study region, where we deployed temporary stations to give a denser station distribution. The path coverage rises to a peak between 10 and 15 s before reducing slowly as the period increases. This offers a robust result between 5 and 30 s where the path coverage is highly dense. In contrast, at shorter and higher periods ($5 >$ period > 30 s) the path coverage is minimal; therefore, the resolution is expected to be relatively low at the depth ranges constrained at these periods. We can infer possible zones with low directional path coverage to fall around the edges where the stations are sparsely distributed. Bearing this in mind, we performed a couple of checkerboard tests to evaluate the resolution of our dataset using the actual data coverage and the robustness of our model as described below.

We generated a layered isotropic model from the average of a 3-D *Vsv* model in each layer. This 3-D *Vsv* model is obtained by combining two different *Vsv* models in the region (Y. Meng et al., 2019; Shen et al., 2016). The combination is necessary since Shen's model is sparse so where velocity values are missing, we make it up with the Y. Meng et al. (2019) model. Positive and negative anomalies of 6% magnitude were allocated interchangeably at the grid nodes to form a checkerboard model. Next, solving Equations 10 and 11 for $\frac{G_s}{L}$ and $\frac{G_c}{L}$, an azimuthal anisotropic input model of amplitude 2% and horizontal anomaly of $1° \times 1°$ was generated between 0 and 30 km and of $1.25° \times 1.25°$ at greater depth beyond 30 km.

The checkerboard patterns have fast axes alternated in the vertical and horizontal directions (Figure 3a). We then perturbed the models by adding 0.5% Gaussian noise into the synthetic interstation Rayleigh wave travel times and retrieved the models following our two-step workflow as described above (Figure 3). This was repeated for a 1%

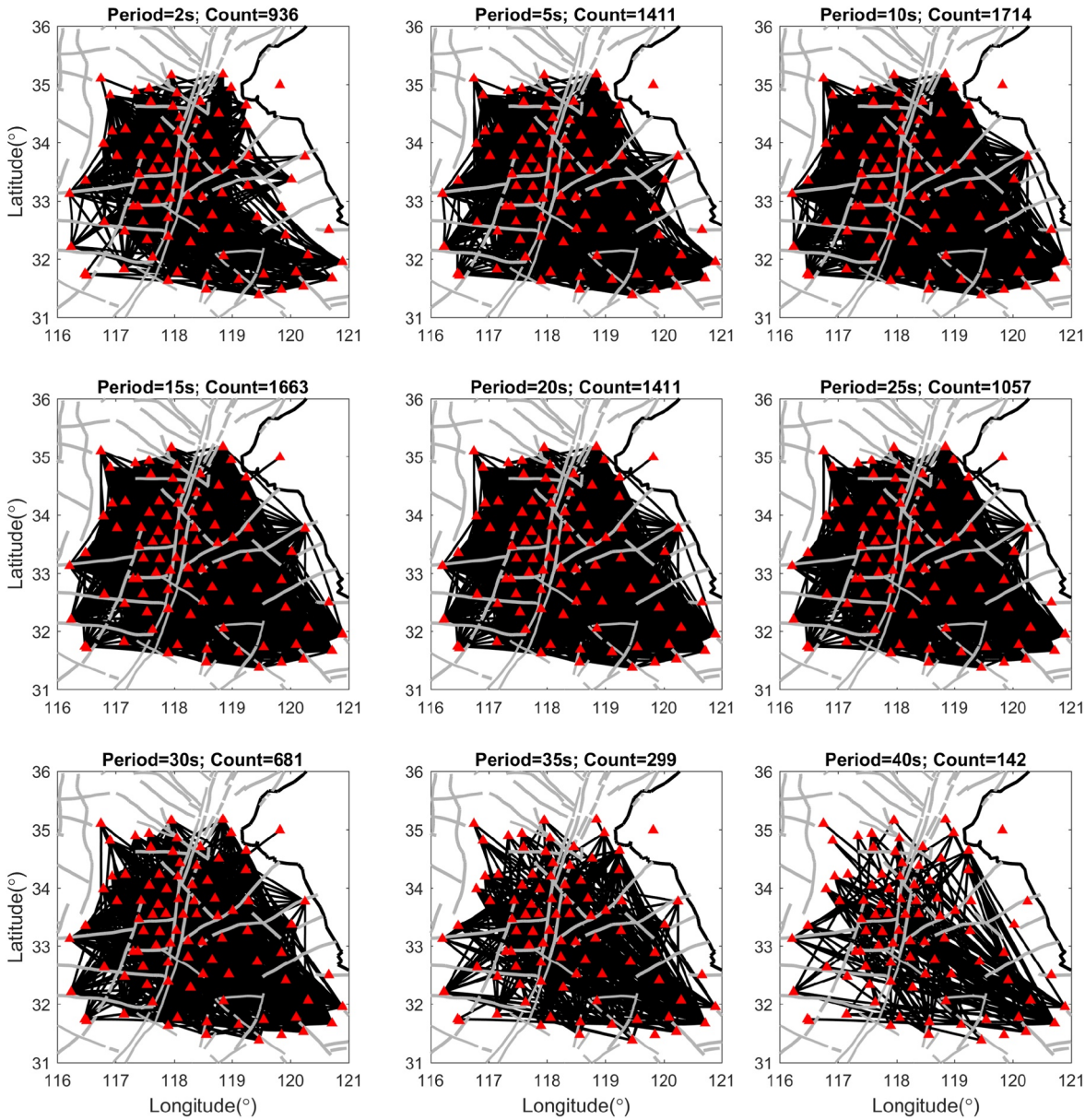

Figure 2. Rayleigh wave phase velocity raypath coverage maps at different periods between 2 and 40 s. The peak count is between 10 and 15 s, while at 2, 35, and 40 s, the path coverage is sparse at the edges. The gray lines are faults.

Gaussian noise level to check the influence of noise level on the model (Figure S3 in Supporting Information S1). Overall, with the checkerboard test, one can get a rough estimate of the noise level tolerance in a given dataset. This means that increasing noise level in a dataset will amplify the uncertainty in the model, and for azimuthal anisotropy, a larger noise level reduces the anisotropic strength (amplitudes) and increases the deviations of anisotropic patterns (C. Liu et al., 2019). Nevertheless, the azimuthally anisotropic *Vsv* could be well recovered for synthetic datasets with 0.5% and 1% Gaussian noise levels within regions with dense raypath coverage.

Joint inversion for isotropic and anisotropic velocity has a critical trade-off issue due to the coupling between isotropic structures and anisotropy of the tomographic inversion. This makes a complicated model that becomes difficult to be recovered without leakages or smearing where data coverage may not be adequate. Compared with conventional tomography for only the 3-D isotropic velocity variations, imaging anisotropy requires a much better directional coverage of seismic rays beside the number of ray hits to stabilize the inversion (Z. Huang

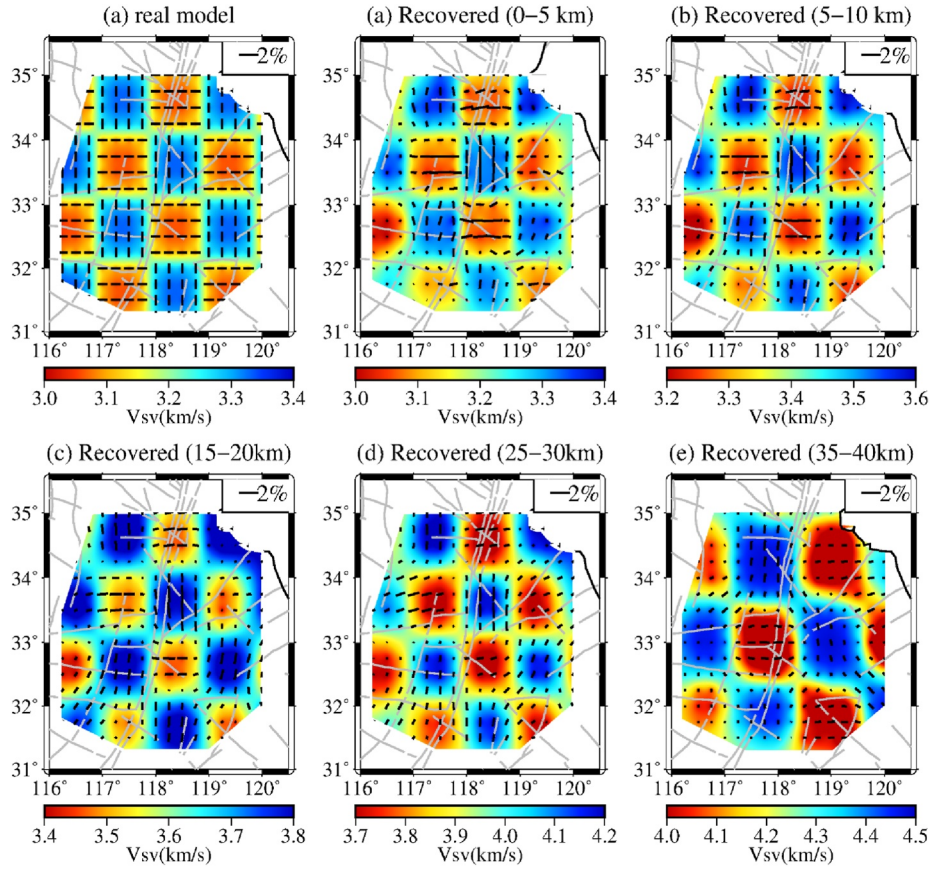

Figure 3. Checkerboard resolution test for coupled isotropic (color bar) and azimuthal anisotropy (black bars) with 0.5% Gaussian noise level and 2% amplitude. The input model (a) has 1° × 1° horizontal anomaly sizes and is recovered as shown (b)–(d), while (e) is the recovered model when the horizontal anomaly size is increased to 1.25° × 1.25°. The directions of the fast axes are given by the strikes of the short black bars obtained by interchanging them between 0° and 90°.

et al., 2015). We observed that the smearing of the isotropic velocities is very weak, and no artifacts were generated. However, we observed smearing of anisotropy in the uppermost mantle depth (30–40 km) with reduced magnitude of anisotropy and increased deviation of fast axes' directions. This can also be observed on the edges where the raypath coverage is not dense enough. In order to improve the recovery, between the depths of 30 and 40, larger anomaly sizes (1.25° × 1.25°) in the horizontal direction were used (Figure 3e and Figure S3e in Supporting Information S1).

We also performed another test (model recovery test), which aims to decipher the uncertainties in the resulting model caused by the noise in the actual data. Here, the obtained isotropic model from the joint inversion was perturbed by adding a 0.5% Gaussian random noise (e.g., Bensen et al., 2008; C. Liu et al., 2019). It was then inverted following the two-step workflow, and recovery of both isotropic and anisotropic *Vsv* was examined for consistency. The results (Figure S4 in Supporting Information S1) are consistent with the checkerboard test results discussed above when compared in the horizontal slice (compare Figure 3 and Figure S4 in Supporting Information S1). Our checkboard test results illustrate that our models are robust and consistent, giving us the confidence for the interpretation (Section 4).

To verify the reliable depth at which materials could influence the characteristics of Rayleigh waves at all the frequencies or periods in our model, we employed a 1-D velocity model sensitivity of Rayleigh wave phase speed perturbations with respect to the perturbations of *L* and *A* for periods between 2 and 40 s (Figure S5 in Supporting Information S1). The normalized results indicate that the period range considered offers excellent sensitivity to structures from the crust up to the depth of 50 km, which is about the depth in the uppermost mantle. The Moho distribution in East China has an average depth between 30 and 35 km in the study region (e.g., Shen et al., 2016;

Teng et al., 2014). We could observe that for the same period of L and A, Rayleigh waves show much higher sensitivity to the deeper structures of L than of A. Shorter periods have the best sensitivity to shallow structures, while the longer period waves are demonstrated to have a more pronounced sensitivity to the deeper structure (see also, C. Liu et al., 2019).

3.2. The Uncertainty in the Azimuthal Anisotropy

Aside from the model resolution, we followed a statistical approach to evaluate the propagation of errors on the model. Since the azimuthal anisotropy inversion is a linearization problem where the targeted parameters (e.g., A_{SV}, ϕ) are obtained from a set of independent parameters (e.g., G_s and G_c), we estimated the uncertainties indirectly. Yuan and Beghein (2018) showed that the uncertainties in A_{SV} and ϕ can be estimated from the error propagation from G_s and G_c on the model, given as (C. Liu et al., 2019; Yuan & Beghein, 2018):

$$\sigma_{A_{Sv}} = \frac{1}{4}\frac{G_c^2\sigma_{G_c}^2 + G_s^2\sigma_{G_s}^2}{G_c^2 + G_s^2},$$
$$\sigma_{\phi} = \frac{1}{4}\frac{G_c^2\sigma_{G_s}^2 + G_s^2\sigma_{G_c}^2}{\left(G_c^2 + G_s^2\right)^2}, \tag{12}$$

where $\sigma_{G_c}^2$ and $\sigma_{G_s}^2$ are the variances of G_c and G_s.

If the data and associated errors follow a Gaussian distribution, it can be shown that G_c and G_s and the associated variances also follow Gaussian distribution. We considered the inversion statistics to verify this condition by comparing the travel-time data residuals (Figure S6 in Supporting Information S1). The results show that the travel time distributions of the initial model varied from about −10 to 10 s, with a mean value of about 0.918 s. After the inversions, the final models improved significantly with the residuals following a Gaussian distribution centered at about 0 s (see the legend in Figure S6a in Supporting Information S1). The spread of the travel time residuals after isotropic and joint inversion for isotropic and anisotropy have over 90% of residuals between −2 and +2 s. Another way is to consider the improvement of the standard deviations with iterations as shown by the significant reduction (Figure S6b in Supporting Information S1). Before the inversion, the standard deviation was 1.96 s but reduced significantly to about 1.45 s after 30 iterations. Although about 30 iterations are considered, we have observed that the inversion system converges just after the first 6–8 iterations, which are enough to guarantee a satisfactory result. It is important to note here that the improvement of the models as shown by comparing the residuals is determined by the starting model. This is one of the reasons for our two-step approach where a stable and reliable *Vsv* model is firstly obtained to serve as a more reliable initial isotropic model for the next step anisotropic inversion, accelerating the convergence of the inversion (C. Liu et al., 2019) and also reducing the trade-off between isotropic and azimuthally anisotropic parameters. However, if a poor initial model is used, the final mode will need a large variation over many iterations to converge.

One of the problems that arise often in geophysical inversion and scientific inquiry, in general, is to quantify the balance of a model complexity with its goodness of data fit. Usually, a plot of the data residuals alone (Figure S6 in Supporting Information S1) cannot give a definitive answer regarding which model performed better statistically. To quantify the goodness of model fitness to data, we have used F-test and Akaike information criterion (AIC). This involves determining how much the misfit of the anisotropic model is significantly lower than that of the isotropic model. The detail is explained in the supplementary information (Text S1 in Supporting Information S1). The results of the F-test and the AIC are consistent, revealing that the anisotropic model does not offer a statically better fit to the data at all periods than the isotropic model. The AIC which places a penalty on over-fitting of models reveals a higher value for the anisotropic model than the isotropic model. This however does not indicate that the anisotropic model is not robust. Generally, we don't expect a very large deviation of the misfit of the anisotropy from the misfit of the isotropic model. This could be attributed to the fact that the inversion of anisotropy is made under the assumption of a weak anisotropic medium (Montagner & Nataf, 1986; Smith & Dahlen, 1973). And the isotropic model may have already fit the data quite well. Thus the improvement of data fitting is usually not significant when we perform joint inversion of both isotropic and azimuthally anisotropic parameters (C. Liu et al., 2019; Z. Zhang et al., 2022). This may limit the variation of the misfit to just a reasonable range enough to give a robust model as also shown by several model resolution tests (Section 3.1).

There are a couple of approaches to estimate the uncertainties on a model indirectly. One way is via the application of the Monte Carlo error propagation technique, in which randomized noisy datasets are inverted and standard deviation calculated (Bem et al., 2020; Fang et al., 2015). We used bootstrap resampling to quantify the uncertainty on the azimuthal anisotropy model. First, we randomly resampled the observed data into 250 ensembles without repetition. This produced about 65% of the original data size in each resampled dataset. Alternatively, resampling of the original data can be done randomly with replacement, thereby producing ensembles of the same size as the original dataset (Rawlinson et al., 2014). Next, the initial models of G_c and G_s were randomly sampled around a zero mean and standard deviation of 1. This is necessary for us to determine the statistical behaviors of G_c and G_s in accordance to Equation 9 above. The inversion is accomplished by fitting predicted travel times to the data by minimizing the chi-squares iteratively. G_c and G_s are solved for iteratively as well, beginning with an initial model. Since we have a prior knowledge of the distributions of G_c and G_s, we can randomly sample them following Gaussian distribution from which variances can be calculated. While keeping the reference model (isotropic), regularization parameters, and grid spacing fixed, the two-step inversion was implemented for the realizations, producing 250 different models. The variances and means of G_c and G_s from the whole realizations were then calculated, from which σ_ϕ and $\sigma_{A_{Sv}}$ were estimated following Equation 9.

The results of the error analysis (Figures 4 and 5) show that the model is stable and robust, judging from the overall small values of the uncertainties. On average, the uncertainties are (<10°) for the direction of fast axes and about 0.2% for the magnitude of anisotropy. However, a few regions on the model have high uncertainties (greater than 15° for the azimuth and about 0.4% magnitude), signifying strong deviations in the anisotropy. The trade-off between anisotropy and heterogeneity affects the amplitude, and the noise in the anisotropic travel times is also amplified when the recovered isotropic model strongly deviates from the actual situation (Z. Huang et al., 2015). C. Liu et al. (2019) conducted a synthetic test to check the impact of sharp velocity contrast or changes on the anisotropy. Their results reveal that while the direct inversion method generally performs well, recovering about 73% of input models, trade-offs were observed at the transition zones. The trade-off between strong heterogeneity and anisotropy resulted in the deviation of fast axes from the input and reduced azimuthal anisotropy's strength (C. Liu et al., 2019). The isotropic velocity model of our study region reveals substantial heterogeneity around these regions (e.g., Bem et al., 2020, Figure 6), which we believe could result in weak anisotropic magnitudes and large deviations of the direction of fast axes. Aside from the effect of heterogeneity, a strong deviation is likely to be observed where minimal directional raypath coverage is observed on the edges.

3.3. 3-D Isotropic *Vsv* and Azimuthal Anisotropy Model

The final isotropic *Vsv* and azimuthal anisotropy models from the upper crust to the uppermost mantle are illustrated in both lateral slices (Figure 6) and vertical transacts (Figure 7) to form a 3-D model. The 3-D model of the study region is constructed on a meshed grid of 0.25° × 0.25° in the horizontal direction and 5 km depth intervals, with the isotropic velocity and azimuthal anisotropy given as the average values between layers. Figure 6a represents the upper crust, which extends from about 0 to 12 km. The strength of anisotropy is moderate in the entire layer, with the strongest values occurring beneath the TLF zone and around other faults in the region. The isotopic *Vsv* is relatively higher beneath the southern NCC than the TLF zone and in the northern SCC, characterized by sedimentary basins. There exist significant lateral variations of the anisotropy in the layer, revealing different anisotropic fabrics that correlate with delineated isotropic *Vsv* provinces that are shown to fit surface geologic and tectonic structures (e.g., Bem et al., 2020). The middle crust covers approximately 12–20 km depth, represented by Figure 6b. The direction of the fast axes in the layer is consistent with the results in the upper crust. However, there is a significant reduction in lateral variation of both isotropic and anisotropic *Vsv*. Majorly, the TLF zone from Zhangbaling uplift to the southeastern SOB is characterized by approximately NNE-SSW-oriented fast axes that coincide with the strike of the fault in the region. This trend separates the WSW-ENE trending fast axes in the western side of the TLF zone from the fast axes in the far eastern side of the study region beneath the Subei and the Sulu basins. One key difference between identified anisotropy in the upper crust and the middle crust is that the dominant NNE-SSW trending fast axes associated with the TLF zone are spread eastward, covering a more significant part of the eastern flank of the TLF zone in the middle crust.

The patterns within the lower crust down to the uppermost mantle are less complex than the observed ones in the upper crust. Figures 6d and 6f represent the lower crust and uppermost mantle. The isotropic *Vsv* in the lower

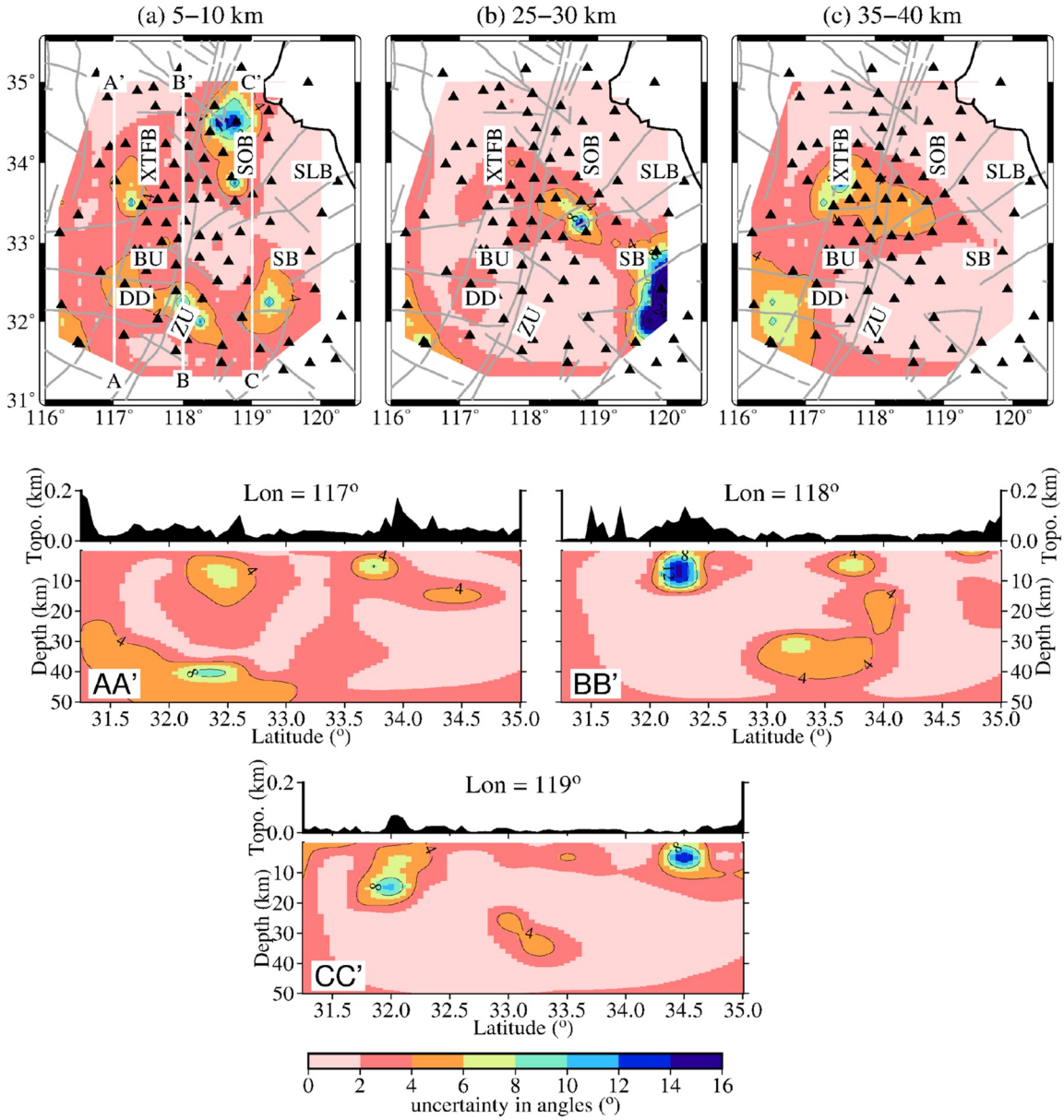

Figure 4. Uncertainties in the angles of azimuthal anisotropy (color bar). Top (a–c) are horizontal slices representing results in the upper crust, the lower crust, and the uppermost mantle, respectively. AA', BB', and CC' are vertical profiles (white lines in slice a). Black triangles are the station distribution with respect to uncertainties.

crust is relatively low in the western side of the TLF zone, beneath the southeastern edge of the NCC. Whereas, in the eastern side of the TLF zone, beneath the northern SCC, the values are comparatively high. This may suggest that the crust is thinner in the SCC than NCC (Figures 6d and 6e). The direction of fast axes in the lower crust and the uppermost mantle are generally unchanged. The dominant NNE-SSW trending fast axes that are characteristic of the strike of the TLF zone still exist in the Zhangbaling uplift. However, the fast axes changed to N-S beneath the SOB and the Xuzhou thrust-and-fold belts in the northern regions in the uppermost mantle (Figure 6f).

The variations of isotropic and anisotropic *Vsv* along five vertical transacts (Figure 7) reveal consistent features as observed in the horizontal slices. The orientation of the fast axes in AA' indicates an approximately WSW-ENE fast axis in the south to Dingyuan depression from the crust to the uppermost mantle. Beneath the Bengbu uplift to Xuzhou thrust-and-fold belt, the fast axes are polarized in the E-W to sub-E-W. The eastern flank of the TLF zone (CC') shows similar orientations of fast axes with profile BB'. This may highlight the strong influence of

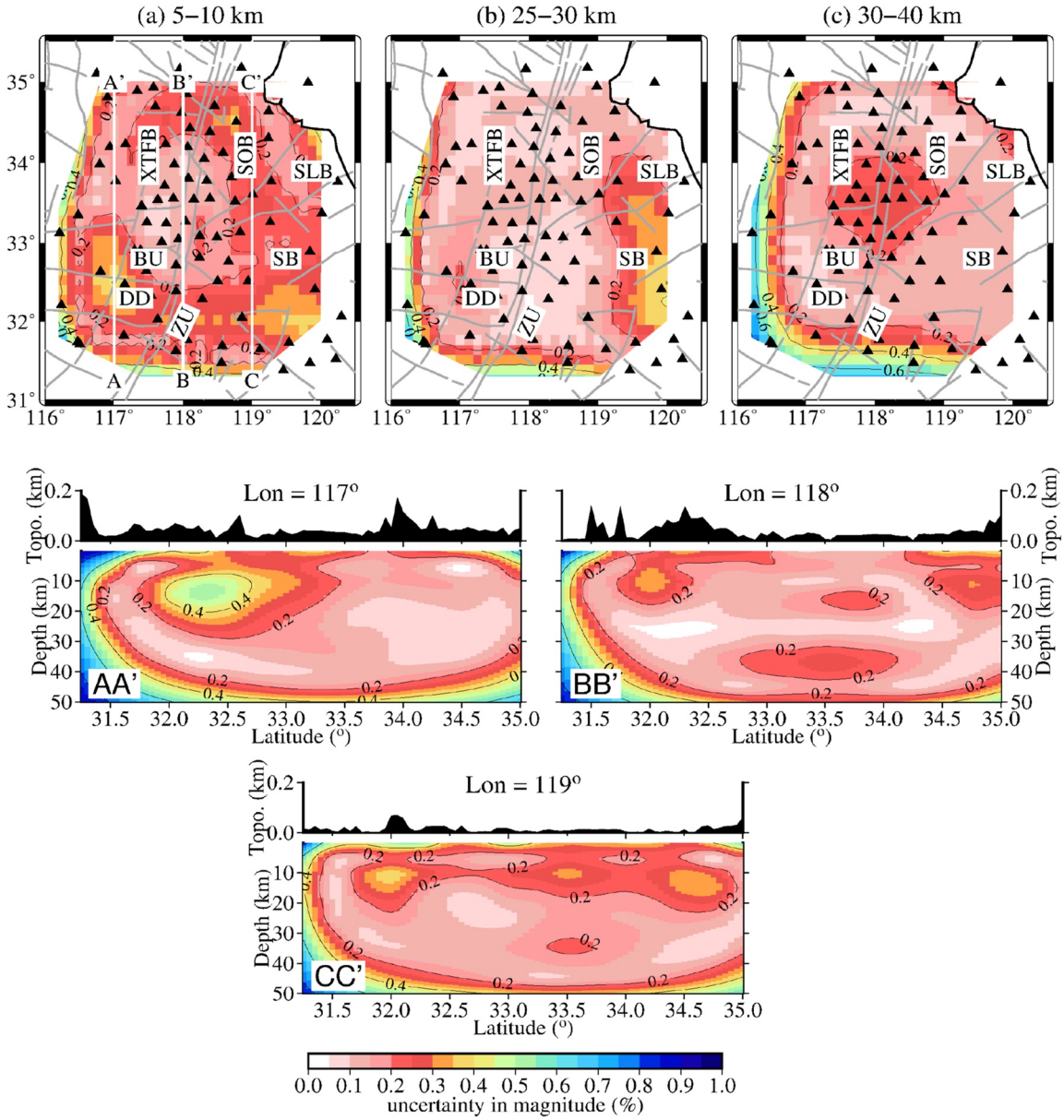

Figure 5. Uncertainties in the amplitudes of azimuthal anisotropy (color bar), with a description as Figure 4.

the TLF zone on the anisotropy in the eastern flank of the fault compared to the observed patterns on the western side. Overall, the orientations are NNE-SSW in the south but change to N-S in the lower crust – uppermost mantle in the north of the profiles. Profiles DD' and EE' cut the TLF zone from E-W, as shown in Figure 6a. Profile DD' shows a consistent NNE-SSW anisotropic pattern beneath the TLF zone and on both sides of the fault, characteristic of the observed anisotropy in the Zhangbaling segment of the TLF zone. Along profile EE', the observed patterns are N-S oriented in the lower crust to the uppermost mantle in the TLF zone. The eastern edge of the profile cut the Sulu basin with a distinct NW-SE anisotropic pattern extending from the upper crust to the uppermost mantle. Meanwhile, the western side of the TLF zone reveals sub-E-W oriented fast axes in the crust. Overall, we can categorize the fast axes of the study region into two main classes: the dominant NNE-SSW to N-S fast axes and the WSW-ENE to E-W. The NNE-SSW to N-S fast axes coincide with the strike of the TLF zone beneath the fault and the eastern flank in the crust and the uppermost mantle, while the observed WSW-ENE to E-W patterns is observed in the western side of the TLF zone.

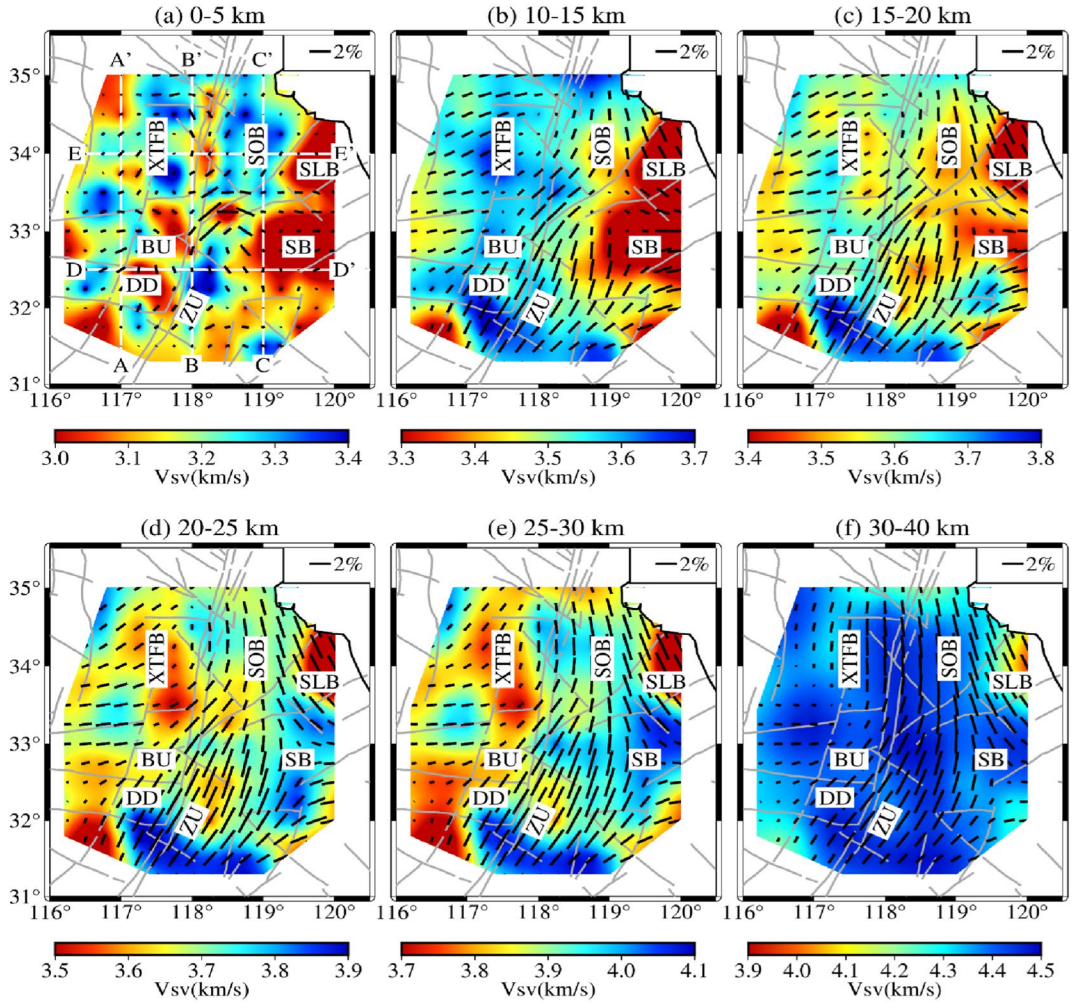

Figure 6. Depth-dependent isotropic phase velocity (color bars) and azimuthal anisotropy (short black bars). The lengths of the bars are proportional to the amplitudes of anisotropy. White lines AA', BB', CC' DD', and EE' are the vertical profiles (Figure 7). Major tectonic units: Xu-Huai Thrust-and-Fold Belt (XTFB), Sulu Orogenic Belt (SOB), Zhangbaling Uplift (ZU), Subei Basin (SB), Sulu Basin (SLB), Dingyuan Depression (DD), Bengbu Uplift (BU), and Tan-Lu Fault (TLF).

4. Discussion

4.1. Comparison of Azimuthal Anisotropy With Other Models

We compare the depth-dependent azimuthal anisotropy with the shear-wave splitting result of X. Yang et al. (2019), the Absolute Plate Motion (APM) computed from the hot spot model (Gripp & Gordon, 2002), and the maximum compressional stress (Heidbach et al., 2018; Figure 8). For clarity of the figure, we used $0.5° \times 0.5°$ gride intervals in the horizontal directions for our model for the comparison. Because the effect of compressional stress is maximum in the upper crust and less in the lower crust and uppermost mantle, we compare the maximum compressional stress field with our model in the upper crust (Figure 8a) and then, in the lower crust and the uppermost mantle, we compare the results of shear-wave splitting, APM and our model (Figures 8b and 8c). In the upper crust, the stress field and anisotropy are approximately in the WSW-ENE direction in the western flank of the TLFZ. This shows a significant correlation between the azimuthal anisotropy model and the maximum compressional stress field. The average stress field does not match our model in the TLF zone from the Zhangbaling uplift in the south to the SOB, where anisotropy coincides with the fault's strike. This may indicate that on the western side of the TLF zone, where we observed a significant correlation between the compressional stress field and anisotropy, the sources of the anisotropy are mainly from the ambient stress field. Generally, the compressional stress representing the first order deformation mechanism could induce cracks that will control the

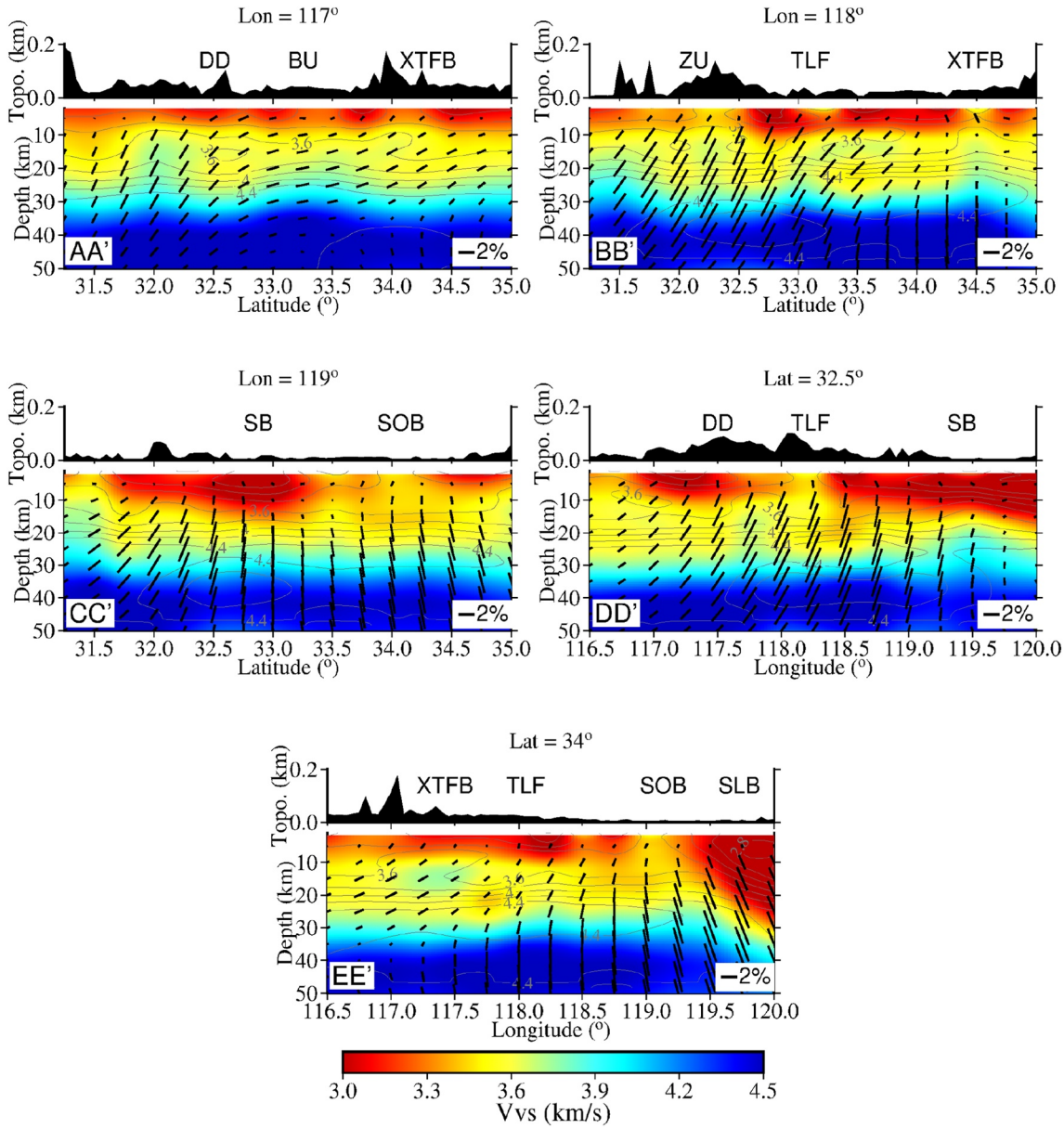

Figure 7. The vertical profiles of isotropic (color bar) and azimuthal anisotropy (short bars). AA', BB', and CC' traverses from the S-N direction while DD' and EE' are in the W-E direction. Major tectonic units are abbreviated on top of the profiles, same as Figure 6.

anisotropy with the fast axes directions aligning with these cracks. In the TLF zone and the SOB, where anisotropy coincides with the fault's strike but not with the compressional stress field, we linked the anisotropy to fault fabrics which may include fractures that strike parallel to the fast axes.

In the lower crust and the uppermost mantle, the directions of fast axes change in the north of the study region, starting from around latitude 33.5°N from NNE-SSW to N-S. Comparing the shear-wave splitting results and the direction of the fast axes revealed that overall, the two models show no correlation with the direction of fast axes of azimuthal anisotropy, particularly in and around the TLF zone. This discrepancy may suggest that the sources of anisotropy constrained by the two datasets and methods are entirely different. By implication, we propose that the observed anisotropy is controlled mainly by dominant lithospheric structures from the crust to the uppermost mantle, while the splitting result reflects deeper upper mantle anisotropic sources, likely at the asthenospheric depths. Other studies have also validated these speculations. For instance, the study of crust and mantle anisotropy from waveform splitting reveals that the crustal contribution usually is very small (in order of

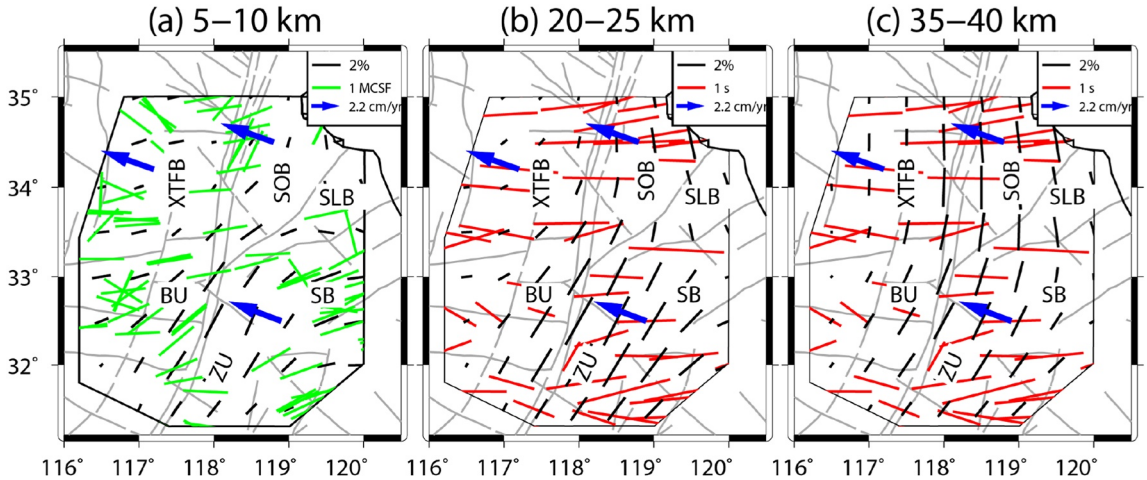

Figure 8. Comparison of azimuthal anisotropy model with other models. In the legend, black, red, and green bars represent the azimuthal anisotropy, shear-wave splitting results (X. Yang et al., 2019), and the local maximum compressional stress field directions (Heidbach et al., 2018), respectively. The blue arrow is the absolute plate motion computed from the hot spot model (Gripp & Gordon, 2002). Comparison of the local maximum compressional stress field directions and the direction of fast axes of azimuthal anisotropy in the upper crust (a). (b) and (c) compare the shear-wave splitting, APM, and fast axes of azimuthal anisotropy in the lower crust and the uppermost mantle.

0.1 s) compared to total delay times of about 1.05 s (Iidaka & Niu, 2001; C. Y. Wang et al., 2017). The average crustal thickness in the study region is about 30 km. Meanwhile, the crustal contribution is expected to be around 0.1 s per 10 km for a deformed crust (Shi et al., 2013). By implication, 30 km thick crust should contribute about 0.3 s delay time against the observed 1.05 s from the mantle.

To probe further the sources of the anisotropy constrained by the two models, we also compare the results with the orientation of the APM in this region (blue arrows). We observed a significant correlation between the APM and the average directions of shear-wave splitting results than our model. This implies that the seismic anisotropy revealed by shear-wave splitting in central East China is a regional feature, most likely controlled by the subduction-related asthenospheric flow, which may align LPO of mantle minerals in the direction of APM. The evolution of the Eastern China lithosphere and the APM is revealed to be controlled mainly by the west-dipping subduction of the paleo-Pacific Plate beneath Eurasia in the Late Triassic and was completed in the early Jurassic following the Meso-Cenozoic collision between the NCC and SCC (D. Chen et al., 2015; Wei et al., 2020; L. Zhao et al., 2013). On the other hand, the anisotropy in the crust and uppermost mantle in the study region is controlled by lithospheric sources that include the maximum compressional stress field beneath the NCC and fault fabrics within proximity of the TLF zone. Clearly, in the TLF zone, the polarization of anisotropy prioritizes the strike of the fault in the crust and the uppermost mantle, which may signify that the TLF cuts through the entire crust into the uppermost mantle, controlling the lithospheric anisotropy in the region.

4.2. Azimuthal Anisotropy and Significance to Lithospheric Deformation

Relatively high lateral variations of *Vsv* (isotropic and anisotropic) exist in the first 10 km of the central-southern TLF zone and adjacent regions. These variations affirm the velocity segmentation reported in velocity tomography of central-eastern China in the upper crust (e.g., Bem et al., 2020; Xiong et al., 2016). Interestingly, the study region is characterized by intense faulting due to the compressional stress field that must have set up the multistage deformational tectonics observed in the region (Luo & Yao, 2021). The stages may include compressional and extensional activities in eastern China during Mesozoic-Cenozoic (Q. R. Meng et al., 2007; Zhu et al., 2004, 2010). Studies have revealed that the TLF underwent a large-scale strike-slip movement in the Early Cretaceous as a feedback effect of a suddenly high speed and oblique subduction of the Izanagi plate (Zhu et al., 2004, 2010). In the Late Cretaceous to Neogene, the fault zone switched to a large-scale extensional belt (Zhu et al., 2004, 2010).

The episodic activation of the fault system is associated with strong to moderate-size earthquakes such as the 1668 magnitude 8.5 Tancheng earthquake and the 1975 magnitude 7.3 Haicheng earthquake (C. Y. Wang et al., 2017;

Zhou et al., 2010) with a seismogenic layer in the brittle upper crust – the middle crust (e.g., Bem et al., 2020; Deng et al., 2013; Z. Zhang et al., 2012). The implication is that extensive faulting and earthquake-related fractures induced by the compressive and extensional stresses in the region that can easily be filled with fluid may likely characterize the fault zone. The orientation of the fast axes coincides majorly with the strike of the faults within proximity. For instance, in the TLF zone, NNE-SSW polarized fast axes fit the NNE-SSW trending TLF, while average sub-E-W fast axes coincide in the west of the TLF zone with the strikes of sub-E-W trending faults. Several studies have demonstrated that the upper crust anisotropy usually shows high lateral variation and originates from fluid-filled cracks (Crampin & Peacock, 2008; C. Y. Wang et al., 2017; Y. Yang et al., 2018). We interpret the direction of fast axes in the upper crust as a consequence of fault fabrics within the fault zones and the effect of widespread compressive and extensional stresses induced in the region from subduction tectonics.

Beyond the upper crust, anisotropy is conserved up to the uppermost mantle, especially in and around the TLF zone. We interpret the fast axes' overall consistent alignment with the fault's strike as the effect of deep fault shearing. This is enhanced by the impact of dragging caused by synchronous sinistral faulting (T. Zhao et al., 2016; Zhu et al., 2009, 2010). Large scale dragging is not reported in the west of the TLF zone beneath the NCC, where anisotropy coincides on average to the maximum compressive stress, but it is observed in the eastern flank in the SCC (Zhu et al., 2009). Such dragging could probably contribute to the alignment of fast axes with the strike of the TLF in the east beyond the fault zone. Studies have shown that the TLF system in the Zhangbaling uplift segment up to the west of SOB is dominated by sinistral brittle and ductile shear belts of the Early Cretaceous with a similar deformation pattern as observed in the SOB (T. Zhao et al., 2014; Zhu et al., 2009). Such shearing in the TLF zone will enhance the preferred mineral orientation, dominated by micacious orientation (Weiss et al., 1999) in the direction of the fault's strike. Crampin and Peacock (2008) also argue that shearing in the fault zones will favor the alignment of the fast axes in any rock. The difficulty lies in distinguishing between stress-induced anisotropy and that due to mineral alignment in sheared fracture zones, particularly when the observed maximum compressive stress aligns to the plane of the geological fabric (Balfour et al., 2005).

Interestingly, this is not our case as the comparison of maximum compressive stress and the anisotropy shows significant contrast in and around the fault zone. This leaves us with only one positive conclusion that the anisotropy in the region's lower crust – uppermost mantle is related to shearing in the TLF zone. It also highlights the strong influence of synchronous sinistral faulting of TLF and the associated episodic activation activities of the fault on the anisotropy featured in the crust to the uppermost mantle in central Eastern China. Shi et al. (2013) also observed a gradual rotation of the fast directions in the vicinity of deep-seated fault structures, with the fast directions becoming more parallel to the fault in the proximity of the fault (Shi et al., 2013).

The TLF is observed to have a sluggish S-shape (Xu et al., 1987). The fast axes in the Zhangbaling uplift segment appear more SSW-NNE, consistent with the strike of the intrusive Zhangbaling Group. As you approach the eastern edge of the SOB and across the Xuzhou thrust-and-fold belt, the orientation is rotated to N-S, especially in the lower crust and the uppermost mantle. The relationship between anisotropy and deformation mechanisms can be complex when multiple mechanisms are coupled (Savage, 1999). For instance, the preferred orientation of Olivine will typically favor the direction of mantle flow but might differ from the direction of plate motion if the plate motion is decoupled (Savage, 1999). Following this idea, we interpret the N-S group across Xuzhou thrust-fold belt to SOB to be the resultant effect of deep sinistral shearing in the TLF zone and the subduction tectonics at the SOB. The subduction at the SOB is inferred to be propelled to the continuous subduction of the Paleo-Pacific Plate in the NW direction (Gripp & Gordon, 2002; J. Wang et al., 2019). This is evident in the NNW-SSE preserved anisotropic fabric in the far eastern Sulu basin with an orientation similar to the subduction. However, the anisotropy is likely to assume the resultant effect of subduction coupled with the deep faulting and shearing in the TLF zone. Even at that, the orientation of the fast axes in the lower crust and uppermost mantle is closely related to the strike of the TLF, signifying the presence of fault movement in the depth range.

4.3. A Possible Geodynamic Model Inferred From Azimuthal Anisotropy

One crucial implication of our observation and interpretation of anisotropic pattern in the TLF zone and adjacent regions in the crust and uppermost mantle is that the TLF zone is a deep lithospheric structure; a piece of information that is vital in resolving the age-long debate about the depth extent of the TLF zone in the south. For instance, Bai and Wang (2006) interpret the lack of apparent velocity anomaly in the fault zone beyond the middle crust as the lack of fault geometry. They speculated that the fault might have cut through the entire crust into the

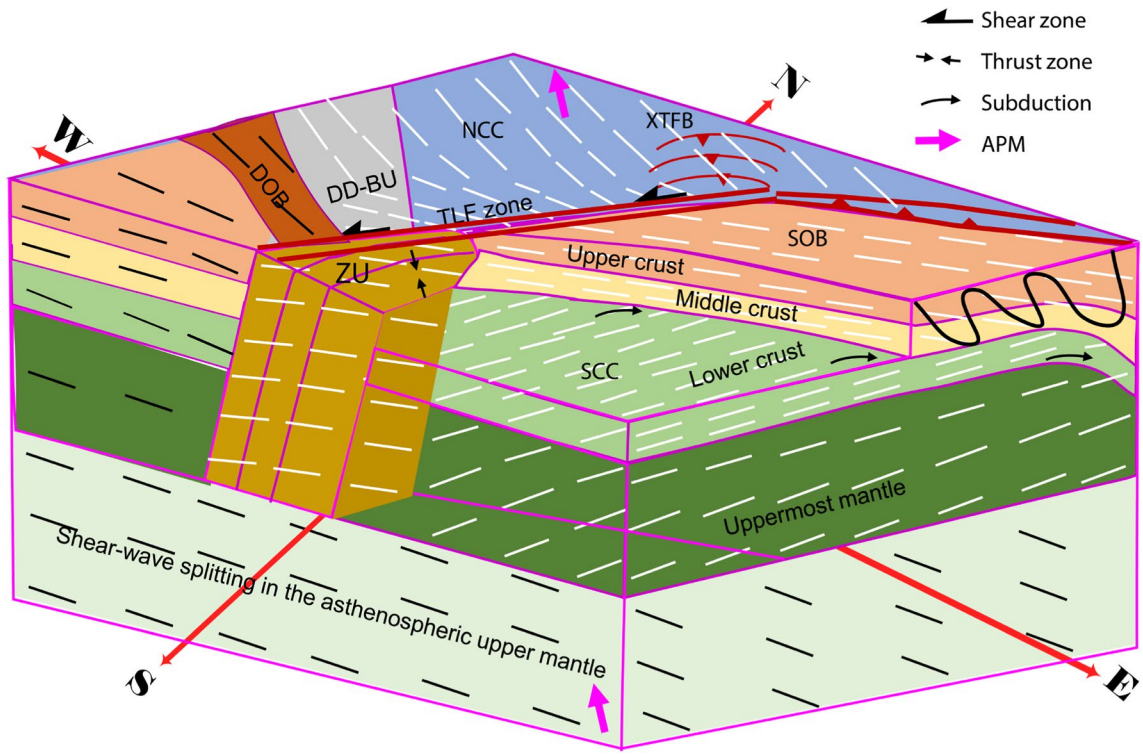

Figure 9. The 3-D schematic representation of the Tan-Lu Fault zone structure, azimuthal anisotropy (short white bars) from the upper crust to the uppermost mantle, and shear-wave splitting results in the upper mantle and DOB region (short black bars) (X. Yang et al., 2019). The average orientation of the splitting results is in the E-W direction. Tectonic belts: Zhangbaling uplift (ZU), Tan-Lu Fault (TLF); Xuzhou Thrust-and-Fold Belt (XTFB), Sulu Orogenic Belt (SOB); North China Craton (NCC), South China Craton (SCC), Dabie Orogenic Belt (DOB), Dingyuang Depression- Bengbu uplift (DD-BU).

uppermost mantle because of the tensile stress field that arose from the regional Moho uplift. But while the fault geometry is preserved in the brittle upper-middle crust, extension during orogenic processes that characterize the south-central segment and crustal adjustment to accommodate the various instability actions must have eroded the fault features in the lower crust (Bai & Wang, 2006). Our observations support the deep penetration of the TLF zone with the direction of the anisotropy preserved in the crust to the uppermost mantle favoring the fault' strike.

Figure 9 gives the pictorial representation of the azimuthal anisotropy model and shear-wave splitting results in the central-southern segment of the TLF zone and adjacent regions. Different models exist for the formation and evolution of the TLF zone. We have summarized these models into three groups based on the timing of the collision of NCC and SCC. These are the pre-collisional models (e.g., Gilder et al., 1999; Watson et al., 1987; Xu et al., 1987; Xu & Zhu, 1994), syn-collisional models (e.g., Li, 1994; Yin & Nie, 1993; T. Zhao et al., 2016; Zhu et al., 2009) and the post-collisional models (e.g., Okay & Celal Şengör, 1992). These models have their strengths and weaknesses. For instance, the pre-collisional fault models do not fit the current geometries of the NCC and SCC along the fault without producing observable contradictions or extensions. Moreover, like the sinistral strike-slip models, some of them cannot explain the abrupt termination of the fault in the eastern edge of the DOB. The syn-collisional models have proven viable but not without contradictions. The syn-subduction transform fault model regards the TLF as a product of vertical, sinistral tearing of the subducted SCC due to differential subduction velocities (Zhu et al., 2009). Similar to the indenter boundary model of Yin and Nie (1993) that favors the SCC with a promontory that thrust into the NCC from the suture boundary of DOB along TLF to SOB, these models could not account for the lack of intense shortening of the NCC at SOB compared to the DOB. T. Zhao et al. (2016) argued that for prolonged and intense impact at SOB as proposed in the indental and syn-subduction transform fault models, one would expect much more occurrence of UHP rocks and higher crustal shortening at SOB compared to DOB that is suggested to have entered the collision late. T. Zhao et al. (2016) proposed an indentation-induced continent-tearing model, which upholds that the present southern boundary of the NCC represents its original shape with a promontory in the northern boundary of the DOB. At the oceanic

subduction stage, the overriding NCC promontory forced a vertical tearing of the subducting oceanic plate along the TLF zone, which formed the eastern boundary of the promontory (T. Zhao et al., 2016). The thrusting of the promontory with the corresponding tearing, folding, and dragging of the SCC lasted at DOB until SCC collided at the SOB.

We aligned our interpretation with the indentation-induced continent-tearing model (T. Zhao et al., 2016) and proposed the thrusting and extension at the DOB between the NCC and SCC in the Meso-Cenozoic is likely the cause of the anisotropy in the southeastern NCC. The northern areas of the DOB remained in extensional tectonic during the Middle to Late Jurassic, coeval with exhumation at the DOB (Q. R. Meng et al., 2007). Such a mechanism is thought to have produced a series of deep and horizontally aligning thrust-and-fold belts in front of the northern edge of the DOB. We believe that the extensional and compressional tectonics in the region are related to the azimuthal anisotropy pattern observed in the region that reflects the ambient stress field. Along the TLF and the Zhangbaling uplift, the dragging of the SCC and the Early Cretaceous extensional movement of the Tan-Lu Fault, which was accompanied by intense magnetism, must have caused the SSW – NNE pattern (Luo et al., 2021; Q. R. Meng et al., 2007). Evidence from the earthquake studies, distribution of syn-collisional structures, and seismic tomography studies (e.g., Bem et al., 2020; Deng et al., 2013; Zhu et al., 2009), suggest that the SCC is less rigid than the NCC. This implies that the SCC was easily dragged during the thrusting and extension of the NCC and SCC in the Meso-Cenozoic. This resulted in the deformation of the marginal areas with anisotropy aligning with the fault's strike as observed in our model in the eastern flank of the TLF zone. Besides, studies of marginal structures show that the TLF controls their shapes and trends in the middle segment (D. Chen et al., 2015; Zhu et al., 2009).

5. Conclusions

This study constrained the depth-dependent isotropic and azimuthal anisotropy *Vsv* in the crust and uppermost mantle in the central-south Tan-Lu fault zone and adjacent regions. The anisotropy *Vsv* model was compared with the other models, such as maximum compressive stress, shear-wave splitting results, and the absolute plate motion. Discussion and the implication of the results to regional deformations were made, from which we made the following conclusions.

1. The characteristic anisotropy is segmented and stratified, suggesting multi-sources, mainly the intense faulting in the upper crust due to compressive stress, the extensional movement, and shearing in the TLF zone in the crust and the uppermost mantle. By comparing azimuthal anisotropy with other models such as the maximum compressive stress field, shear-wave splitting, and absolute plate motion, we observed that the anisotropy is generally different from these models. However, its direction favors the average strike of the major faults, enabling us to distinguish between stress- and structure-related anisotropy
2. In the upper crust, the anisotropy in the TLF zone and its margin is linked to fault fabrics, possibly characterized by large-scale cracks striking in the same direction with the direction of fast axes. In the western side of the TLF zone, where anisotropy shows a significant relationship with the direction of maximum compressive stress, we ascribed the source to ambient differential stresses in terms of anisotropic crack compliance
3. Beyond the upper crust, the primary source of anisotropy is the deeply seated TLF revealed by the NNE-SSW and N-S polarized fast axes. Such is thought to be induced by the ductile (south) and brittle (north) shearing at depth in the TLF zone, which confirms that the fault is a deep-seated lithospheric fault
4. The anisotropy in the central-southern TLF zone suggests a possible indentation-induced continent-tearing model, with compressive stress at the DOB controlling anisotropy in the southern NCC. At the same time, structural causes influenced anisotropy in the TLF zone and the adjacent SCC. The results also suggest that the SCC must have suffered a larger deformation than the NCC in the Meso-Cenozoic

Data Availability Statement

The data of the temporary array stations can be available by request through the China Seismic Array Data Management Center at the Institute of Geophysics, China Earthquake Administration. The Z-Z component of the computed cross-correlation functions used for dispersion analysis is available at (http://dx.doi.org/10.17632/smt379mfwz.1).

Acknowledgments
We acknowledge the Data Management Centre of the China National Seismic Network at the Institute of Geophysics (SEISDMC, doi:10.11998/SeisDmc/SN, http://www.seisdmc.ac.cn), China Earthquake Networks Center, China Earthquake Administration for providing continuous waveform data of the permanent stations. We appreciate Dr. Xiaoyu Yang for providing the shear-wave splitting results for comparison, which can be obtained as supplementary material (https://doi.org/10.1093/gji/ggz242). This study was funded by the National Natural Science Foundation of China (42125401, 41790464), the Strategic Priority Research Program of the Chinese Academy of Sciences (Grant No. XDB41000000), China Postdoctoral Science Foundation (BH2080000099), and the LU JIAXI International team program supported by the KC Wong Education Foundation and CAS (GJTD-2018-12). The first author acknowledges the Ph.D. fellowship received from the Chinese Academy of Science (CAS) and The World Academy of Sciences (TWAS), and Federal University Dutse, Nigeria, for granting him the study leave for his Ph.D. at the University of Science and Technology of China.

References

Bai, Z., & Wang, C. (2006). Crustal P-wave velocity structure in Lower Yangtze region: Reinterpretation of Fuliji-Fengxian deep seismic sounding profile. *Chinese Science Bulletin*, *51*(19), 2391–2400. https://doi.org/10.1007/s11434-006-2115-z

Balfour, N. J., Savage, M. K., & Townend, J. (2005). Stress and crustal anisotropy in Marlborough, New Zealand: Evidence for low fault strength and structure-controlled anisotropy. *Geophysical Journal International*, *163*(3), 1073–1086. https://doi.org/10.1111/j.1365-246X.2005.02783.x

Bem, T. S., Yao, H., Luo, S., Yang, Y., Wang, X., Wang, X., et al. (2020). High-resolution 3-D crustal shear-wave velocity model reveals structural and seismicity segmentation of the central-southern Tanlu Fault zone, eastern China. *Tectonophysics*, *778*(2019), 1–17. https://doi.org/10.1016/j.tecto.2020.228372

Bensen, G. D., Ritzwoller, M. H., & Shapiro, N. M. (2008). Broadband ambient noise surface wave tomography across the United States. *Journal of Geophysical Research*, *113*, 1–21. https://doi.org/10.1029/2007JB005248

Boness, N. L., & Zoback, M. D. (2006). Mapping stress and structurally controlled crustal shear velocity anisotropy in California. *Geology*, *34*(10), 825–828. https://doi.org/10.1130/G22309.1

Chen, D., Zhang, F., Chen, H., Dilek, Y., Yang, S., Meng, Q., & Yang, C. (2015). Structural architecture and tectonic evolution of the Fangzheng sedimentary basin (NE China), and implications for the kinematics of the Tan-Lu fault zone. *Journal of Asian Earth Sciences*, *106*, 34–48. https://doi.org/10.1016/j.jseaes.2015.02.028

Chen, L., Jiang, M., Yang, J., Wei, Z., Liu, C., & Ling, Y. (2014). Presence of an intralithospheric discontinuity in the central and western North China Craton: Implications for destruction of the craton. *Geology*, *42*(3), 223–226. https://doi.org/10.1130/G35010.1

Chen, L., Zheng, T., & Xu, W. (2006). A thinned lithospheric image of the Tanlu Fault Zone, eastern China: Constructed from wave equation based receiver function migration. *Journal of Geophysical Research*, *111*(B9), B09312. https://doi.org/10.1029/2005JB003974

Cheng, C., Chen, L., Yao, H., Jiang, M., & Wang, B. (2013). Distinct variations of crustal shear wave velocity structure and radial anisotropy beneath the North China Craton and tectonic implications. *Gondwana Research*, *23*(1), 25–38. https://doi.org/10.1016/j.gr.2012.02.014

Crampin, S., & Peacock, S. (2008). A review of the current understanding of seismic shear-wave splitting in the Earth's crust and common fallacies in interpretation. *Wave Motion*, *45*, 675–722. https://doi.org/10.1016/j.wavemoti.2008.01.003

Deng, Y., Fan, W., Zhang, Z., & Badal, J. (2013). Geophysical evidence on segmentation of the Tancheng-Lujiang fault and its implications on the lithosphere evolution in East China. *Journal of Asian Earth Sciences*, *78*, 263–276. https://doi.org/10.1016/j.jseaes.2012.11.006

Fang, H., Yao, H., Zhang, H., Huang, Y., & Hilst, R. D. V. (2015). Direct inversion of surface wave dispersion for three-dimensional shallow crustal structure based on ray tracing: Methodology and application. *Geophysical Journal International*, *201*, 1251–1263. https://doi.org/10.1093/gji/ggv080

Faure, M., Lin, W., Monié, P., Le Breton, N., Poussineau, S., Panis, D., & Deloule, E. (2003). Exhumation tectonics of the ultrahigh-pressure metamorphic rocks in the Qinling orogen in east China: New petrological-structural-radiometric insights from the Shandong Peninsula. *Tectonics*, *22*(3), 1–n. https://doi.org/10.1029/2002TC001450

Fouch, J. M., & Rondenay, S. (2006). Seismic anisotropy beneath stable continental interiors. *Physics of the Earth and Planetary Interiors*, *158*, 292–320. https://doi.org/10.1016/j.pepi.2006.03.024

Fu, V. Y., Gao, Y., Li, A., Lu, L., Shi, Y., & Zhang, Y. (2016). The anisotropic structure in the crust in the northern part of North China from ambient seismic noise tomography. *Geophysical Journal International*, *204*, 1649–1661. https://doi.org/10.1093/gji/ggv549

Gilder, S. A., Leloup, P. H., Courtillot, V., Chen, Y., Coe, R. S., Zhao, X., et al. (1999). Tectonic evolution of the Tancheng-Lujiang (Tan-Lu) fault via middle Triassic to early Cenozoic paleomagnetic data. *Journal of Geophysical Research: Solid Earth*, *104*(B7), 15365–15390. https://doi.org/10.1029/1999JB900123

Gripp, A. E., & Gordon, R. G. (2002). Young tracks of hotspots and current plate velocities. *Geophysical Journal International*, *150*(2), 321–361. https://doi.org/10.1046/j.1365-246X.2002.01627.x

Hacker, B. R., Ratschbacher, L., Webb, L., McWilliams, M. O., Ireland, T., Calvert, A., et al. (2000). Exhumation of ultrahigh-pressure continental crust in east central China: Late Triassic-Early Jurassic tectonic unroofing. *Journal of Geophysical Research: Solid Earth*, *105*(B6), 13339–13364. https://doi.org/10.1029/2000JB900039

Hansen, P. C., Jensen, T. K., & Rodriguez, G. (2007). An adaptive pruning algorithm for the discrete L-curve criterion. *Journal of Computational and Applied Mathematics*, *198*(2), 483–492. https://doi.org/10.1016/j.cam.2005.09.026

Heidbach, O., Rajabi, M., Cui, X., Fuchs, K., Müller, B., Reinecker, J., et al. (2018). The World Stress Map database release 2016: Crustal stress pattern across scales. *Tectonophysics*, *744*(April), 484–498. https://doi.org/10.1016/j.tecto.2018.07.007

Huang, H., Huang, Z., Wang, P., Mi, N., Li, H., Yu, D., et al. (2013). Distinct lateral variations of upper mantle anisotropy beneath eastern China revealed by shear-wave splitting. *Geochemistry, Geophysics, Geosystem*, *14*(6), 1842–1855. https://doi.org/10.1002/ggge.20126

Huang, Z., Zhao, D., & Liu, X. (2015). On the trade-off between seismic anisotropy and heterogeneity: Numerical simulations and application to Northeast Japan. *Journal of Geophysical Research: Solid Earth*, *120*(5), 3255–3277. https://doi.org/10.1002/2014JB011784

Iidaka, T., & Niu, F. (2001). Mantle and crust anisotropy in the eastern China region inferred from waveform splitting of SKS and PpSms. *Earth Planets and Space*, *53*(3), 159–168. https://doi.org/10.1186/BF03352373

Li, Z.-X. (1994). Collision between the North and South China blocks: A crustal-detachment model for suturing in the region east of the Tanlu fault. *Geology*, *22*, 739–742. https://doi.org/10.1130/0091-7613(1994)022<0739:CBTNAS>2.3.CO;2

Lin, A., Miyata, T., & Wan, T. (1998). Tectonic characteristics of the central segment of the Tancheng–Lujiang fault zone, Shandong Peninsula, eastern China. *Tectonophysics*, *293*(1–2), 85–104. https://doi.org/10.1016/S0040-1951(98)00087-0

Liu, C., Yao, H., Yang, H., Shen, W., Fang, H., Hu, S., & Qiao, L. (2019). Direct inversion for three-dimensional shear wave speed azimuthal anisotropy based on surface wave ray tracing: Methodology and application to Yunnan, Southwest China. *Journal of Geophysical Research: Solid Earth*, *124*(11), 11394–11413. https://doi.org/10.1029/2018JB016920

Liu, Z., Huang, J., & Yao, H. (2016). Anisotropic Rayleigh wave tomography of Northeast China using ambient seismic noise. *Physics of the Earth and Planetary Interiors*, *256*, 37–48. https://doi.org/10.1016/j.pepi.2016.05.001

Luo, S., & Yao, H. (2021). Multistage tectonic evolution of the Tanlu fault: Insights from upper crustal azimuthal anisotropy of the Chao Lake segment. *Tectonophysics*, *806*(February), 228795. https://doi.org/10.1016/j.tecto.2021.228795

Luo, S., Yao, H., Wang, J., Wang, K., & Liu, B. (2021). Direct inversion of surface wave dispersion data with multiple-grid parameterizations and its application to a dense array in Chao Lake, eastern China. *Geophysical Journal International*, *225*, 1432–1452. https://doi.org/10.1093/gji/ggab036

Meng, Q. R., Li, S. Y., & Li, R. W. (2007). Mesozoic evolution of the Hefei basin in eastern China: Sedimentary response to deformations in the adjacent Dabieshan and along the Tanlu fault. *Bulletin of the Geological Society of America*, *119*(7–8), 897–916. https://doi.org/10.1130/B25931.1

Meng, Y., Yao, H., Wang, X., Li, L., Feng, J., Hong, D., & Wang, X. (2019). Crustal velocity structure and deformation features in the central-southern segment of Tanlu fault zone and its adjacent area from ambient noise tomography. *Chinese Journal of Geophysics*, *62*(7), 2490–2509. https://doi.org/10.6038/cjg2019M0189

Montagner, J. P., & Nataf, H. C. (1986). A simple method for inverting the azimuthal anisotropy of surface waves. *Journal of Geophysical Research*, *91*(B1), 511–520. https://doi.org/10.1029/JB091iB01p00511

Okay, A. I., & Celal Şengör, A. M. (1992). Evidence for intracontinental thrust-related exhumation of the ultra-high-pressure rocks in China. *Geology*, *20*(5), 4112. https://doi.org/10.1130/0091-7613(1992)020<0411:efitre>2.3.co;2

Paige, C. C., & Saunders, M. A. (1982). Lsqr: An algorithm for sparse linear equations and sparse least squares. *ACM Transactions on Mathematical Software*, *8*(1), 43–71. https://doi.org/10.1145/355984.355989

Rawlinson, N., Fichtner, A., Sambridge, M., & Young, M. K. (2014). Seismic tomography and the assessment of uncertainty. *Advances in Geophysics*, *55*, 1–76. https://doi.org/10.1016/bs.agph.2014.08.001

Rawlinson, N., & Sambridge, M. (2004). Wave front evolution in strongly heterogeneous layered media using the fast marching method. *Geophysical Journal International*, *156*(3), 631–647. https://doi.org/10.1111/j.1365-246X.2004.02153.x

Savage, M. K. (1999). Seismic anisotropy and mantle deformation: What have we learned from shear wave splitting? *Reviews of Geophysics*, *37*(98), 65–106. https://doi.org/10.1029/98rg02075

Shen, W., Ritzwoller, M. H., Kang, D., Kim, Y. H., Lin, F. C., Ning, J., et al. (2016). A seismic reference model for the crust and uppermost mantle beneath China from surface wave dispersion. *Geophysical Journal International*, *206*(2), 954–979. https://doi.org/10.1093/gji/ggw175

Shi, D., Lü, Q., Xu, W., Yan, J., Zhao, J., Dong, S., & Chang, Y. (2013). Crustal structure beneath the middle-lower Yangtze metallogenic belt in East China: Constraints from passive source seismic experiment on the Mesozoic intra-continental mineralization. *Tectonophysics*, *606*, 48–59. https://doi.org/10.1016/j.tecto.2013.01.012

Shu, L., Yin, H., Faure, M., & Chen, Y. (2017). Mesozoic intracontinental underthrust in the SE margin of the North China Block: Insights from the Xu-Huai thrust-and-fold belt. *Journal of Asian Earth Sciences*, *141*, 161–173. https://doi.org/10.1016/j.jseaes.2016.08.020

Smith, M. L., & Dahlen, F. A. (1973). The azimuthal dependence of love and Rayleigh wave propagation in a slightly anisotropic medium. *Journal of Geophysical Research*, *78*(17), 3321–3333. https://doi.org/10.1029/JB078i017p03321

Teng, J., Deng, Y., Badal, J., & Zhang, Y. (2014). Moho depth, seismicity and seismogenic structure in China mainland. *Tectonophysics*, *627*, 108–121. https://doi.org/10.1016/j.tecto.2013.11.008

Tian, X., & Santosh, M. (2015). Fossilized lithospheric deformation revealed by teleseismic shear wave splitting in eastern China. *Geological Society of America Today*, *25*(2), 4–10. https://doi.org/10.1130/GSATG220A.1

Wang, C. Y., Wu, Q. J., Duan, Y. H., Wang, Z. S., & Lou, H. (2017). Crustal and upper mantle structure and deep tectonic genesis of large earthquakes in North China. *Science China Earth Sciences*, *60*(5), 821–857. https://doi.org/10.1007/s11430-016-9009-1

Wang, J., Chang, S. C., Chen, Y., & Yan, S. (2019). Early Cretaceous transpressional and transtensional tectonics straddling the Sulu orogenic belt, East China. *Geoscience Frontiers*, *10*(6), 2287–2300. https://doi.org/10.1016/j.gsf.2019.04.007

Watson, M. P., Hayward, A. B., Parkinson, D. N., & Zhang, Z. M. (1987). Plate tectonic history, basin development and petroleum source rock deposition onshore China. *Marine and Petroleum Geology*, *4*(3), 205–225. https://doi.org/10.1016/0264-8172(87)90045-6

Wei, Z., Chu, R., Chen, L., & Wu, S. (2020). Crustal structure in the middle-southern segments of the Tanlu Fault Zone and adjacent regions constrained by multifrequency receiver function and surface wave data. *Physics of the Earth and Planetary Interiors*, *301*, 106470. https://doi.org/10.1016/j.pepi.2020.106470

Weiss, T., Siegesmund, S., Rabbel, W., Bohlen, T., & Pohl, M. (1999). Seismic velocities and anisotropy of the lower continental crust: A review. *Pure and Applied Geophysics*, *156*(1–2), 97–122. https://doi.org/10.1007/s000240050291

Xiong, Z., Li, Q.-H., Zhang, Y.-S., Bi, X.-M., & Jin, S.-M. (2016). Segmentation of crustal velocity structure beneath the Shandong-Jiangsu-Anhui segment of the Tanlu Fault Zone and adjacent areas and its geological interpretations. *Chinese Journal of Geophysics*, *59*(6), 691–702. https://doi.org/10.1002/cjg2.30017

Xu, J., & Zhu, G. (1994). Tectonic models of the Tan-Lu Fault Zone, eastern China. *International Geology Review*, *36*(8), 771–784. https://doi.org/10.1080/00206819409465487

Xu, J., Zhu, G., Tong, W., Cui, K., & Liu, Q. (1987). Formation and evolution of the Tancheng-Lujiang wrench fault system: A major shear system to the northwest of the Pacific Ocean. *Tectonophysics*, *134*(4), 273–310. https://doi.org/10.1016/0040-1951(87)90342-8

Yang, X., Li, H., Li, Y., Lü, Q., Zhang, G., Jiang, G., & Li, X. (2019). Seismic anisotropy beneath eastern China from shear wave splitting. *Geophysical Journal International*, *218*(3), 1642–1651. https://doi.org/10.1093/gji/ggz242

Yang, Y., Yao, H., Zhang, P., & Chen, L. (2018). Crustal azimuthal anisotropy in the trans-North China orogen and adjacent regions from receiver functions. *Science China Earth Sciences*, *61*(7), 903–913. https://doi.org/10.1007/s11430-017-9209-9

Yao, D., Haigang, Z., Peng, Z., Yuanyuan, Y., Xingzhou, W., Peng, M., et al. (2017). New activity of the Tanlu Fault Zone in the south of Huaihe to the Nvshanhu segment since the late Quaternary. *Earthquake Research in China*, *31*(2), 225–233.

Yao, D., Yang, Y., Zhao, P., Shen, X., Fang, L., Shu, P., & Zheng, H. (2016). Microscopic evidence of new activities since late Quaternary in northern Suqian of Tancheng- Lujiang Fault zone. *Progress in Geophysics*, *31*(3), 1017–1026. https://doi.org/10.6038/pg20160312

Yao, H. (2015). A method for inversion of layered shear wavespeed azimuthal anisotropy from Rayleigh wave dispersion using the Neighborhood Algorithm. *Earthquake Science*, *28*(1), 59–69. https://doi.org/10.1007/s11589-014-0108-6

Yao, H., van der Hilst, R. D., & Montagner, J.-P. (2010). Heterogeneity and anisotropy of the lithosphere of SE Tibet from surface wave array tomography. *Journal of Geophysical Research*, *115*(B12), B12307. https://doi.org/10.1029/2009JB007142

Yin, A., & Nie, S. (1993). An indentation model for the North and South China collision and the development of the Tan-Lu and Honam Fault systems, eastern asia. *Tectonics*, *12*(4), 801–813. https://doi.org/10.1029/93TC00313

Yuan, K., & Beghein, C. (2018). A Bayesian method to quantify azimuthal anisotropy model uncertainties: Application to global azimuthal anisotropy in the upper mantle and transition zone. *Geophysical Journal International*, *213*(1), 603–622. https://doi.org/10.1093/gji/ggy004

Zhang, J., Hao, T., Dong, S., Chen, X., Cui, J., Yang, X., et al. (2015). The structural and tectonic relationships of the major fault systems of the Tan-Lu fault zone, with a focus on the segments within the North China region. *Journal of Asian Earth Sciences*, *110*, 85–100. https://doi.org/10.1016/j.jseaes.2014.11.011

Zhang, Z., Wu, J., Deng, Y., Teng, J., Zhang, X., Chen, Y., & Panza, G. (2012). Lateral variation of the strength of lithosphere across the eastern North China Craton: New constraints on lithospheric disruption. *Gondwana Research*, *22*(3–4), 1047–1059. https://doi.org/10.1016/j.gr.2012.03.006

Zhang, Z., Yao, H., Wang, W., & Liu, C. (2022). 3-D crustal azimuthal anisotropy reveals multi-stage deformation processes of the Sichuan Basin and its adjacent area, SW China. *Journal of Geophysical Research: Solid Earth*, *127*, e2021JB023289. https://doi.org/10.1029/2021jb023289

Zhao, L., Zheng, T., & Lu, G. (2013). Distinct upper mantle deformation of cratons in response to subduction: Constraints from SKS wave splitting measurements in eastern China. *Gondwana Research*, *23*(1), 39–53. https://doi.org/10.1016/j.gr.2012.04.007

Zhao, P., Yao, D., Zheng, Y., Yang, H., Peng, M., Li, J., & Shu, P. (2018). The Ziyang Hill Trenches in the anhui Mingguang section of the Tan-Lu Fault Zone and their significance (in Chinese). *Earthquake Research in China*, *34*(4), 642–651. Retrieved from http://www.cnki.net

Zhao, T., Zhu, G., Lin, S., & Wang, H. (2016). Indentation-induced tearing of a subducting continent: Evidence from the Tan-Lu Fault Zone, east China. *Earth-Science Reviews*, *152*, 14–36. https://doi.org/10.1016/j.earscirev.2015.11.003

Zhao, T., Zhu, G., Lin, S., Yan, L., & Jiang, Q. (2014). Protolith ages and deformation mechanism of metamorphic rocks in the Zhangbaling uplift segment of the Tan-Lu Fault Zone. *Science China Earth Sciences*, *57*(11), 2740–2757. https://doi.org/10.1007/s11430-014-4959-4

Zhou, C., Diao, G., Geng, J., Li, Y., Xu, P., Hu, X., & Feng, X. (2010). Fault plane parameters of Tancheng M8½ earthquake on the basis of present-day seismological data. *Earthquake Science*, *23*(6), 567–576. https://doi.org/10.1007/s11589-010-0756-0

Zhu, G., Liu, G. S., Niu, M. L., Xie, C. L., Wang, Y. S., & Xiang, B. (2009). Syn-collisional transform faulting of the Tan-Lu fault zone, East China. *International Journal of Earth Sciences*, *98*(1), 135–155. https://doi.org/10.1007/s00531-007-0225-8

Zhu, G., Niu, M., Xie, C., & Wang, Y. (2010). Sinistral to normal faulting along the Tan-Lu Fault Zone: Evidence for geodynamic switching of the East China continental margin. *The Journal of Geology*, *118*(3), 277–293. https://doi.org/10.1086/651540

Zhu, G., Wang, D., Liu, C., Niu, G., & Song, M. (2004). Evolution of the Tan-Lu Fault Zone and its response to the movement of the western Pacific basin. *Chinese Journal of Geology*, *1*.